Cancer & Metabolism

RESEARCH Open Access

Similar deficiencies, different outcomes: succinate dehydrogenase loss in adrenal medulla vs. fibroblast cell culture models of paraganglioma

Fatimah J. Al Khazal[1,2†], Sanjana Mahadev Bhat[3†], Yuxiang Zhu[4], Cristina M. de Araujo Correia[5], Sherry X. Zhou[1,6], Brandon A. Wilbanks[1,2], Clifford D. Folmes[4], Gary C. Sieck[3], Judith Favier[7] and L. James Maher III[2*]

Abstract

Heterozygosity for loss-of-function alleles of the genes encoding the four subunits of succinate dehydrogenase (SDHA, SDHB, SDHC, SDHD), as well as the SDHAF2 assembly factor predispose affected individuals to pheochromocytoma and paraganglioma (PPGL), two rare neuroendocrine tumors that arise from neural crest-derived paraganglia. Tumorigenesis results from loss of the remaining functional *SDHx* gene copy, leading to a cell with no functional SDH and a defective tricarboxylic acid (TCA) cycle. It is believed that the subsequent accumulation of succinate competitively inhibits multiple dioxygenase enzymes that normally suppress hypoxic signaling and demethylate histones and DNA, ultimately leading to increased expression of genes involved in angiogenesis and cell proliferation. Why SDH loss is selectively tumorigenic in neuroendocrine cells remains poorly understood. In the absence of SDH-loss tumor-derived cell models, the cellular burden of SDH loss and succinate accumulation have been investigated through conditional knockouts of SDH subunits in pre-existing murine or human cell lines with varying degrees of clinical relevance. Here we characterize two available murine SDH-loss cell lines, immortalized adrenally-derived premature chromaffin cells vs. immortalized fibroblasts, at a level of detail beyond that currently reported in the literature and with the intention of laying the foundation for future investigations into adaptive pathways and vulnerabilities in SDH-loss cells. We report different mechanistic and phenotypic manifestations of SDH subunit loss in the presented cellular contexts. These findings highlight similarities and differences in the cellular response to SDH loss between the two cell models. We show that adrenally-derived cells display more severe morphological cellular and mitochondrial alterations, yet are unique in preserving residual Complex I function, perhaps allowing them to better tolerate SDH loss, thus making them a closer model to SDH-loss PPGL relative to fibroblasts.

(281 words)

†Fatimah J. Al Khazal and Sanjana Mahadev Bhat are are co-first authors.

*Correspondence:
L. James Maher III
maher@mayo.edu

Full list of author information is available at the end of the article

Keywords Succinate dehydrogenase, Pheochromocytoma, Paraganglioma, Tricarboxylic acid cycle, Hypoxia, Complex I

Introduction

Succinate dehydrogenase (SDH), is a crucial enzyme complex that catalyzes the oxidation of succinate to fumarate as part of the tricarboxylic acid (TCA) cycle, coupled to reduction of ubiquinone to ubiquinol as Complex II of the mitochondrial electron transport chain [1, 2]. SDH consists of four subunits: SDHA, SDHB, SDHC, and SDHD, and involves assembly factors required for covalent flavinylation of SDHA and iron-sulfur cluster modification of SDHB [3–5]. Deleterious variants in any of the genes encoding these proteins can disrupt SDH enzyme activity, affecting the mitochondrial respiratory chain and normal cellular energy production [6]. While SDH-loss cells are presumably metabolically disabled, it is fascinating that SDH loss can lead to tumors such as gastrointestinal stromal tumor (GIST), renal cell carcinoma (RCC), pituitary neuroendocrine tumors [7] and pheochromocytoma and paraganglioma (PPGL) [8–13]. In these rare tumors SDH-loss metabolism appears to be the primary cause of neoplasia.

Several mechanistic hypotheses have been proposed to connect SDH loss to PPGL tumorigenesis [14–17]. When SDH is deficient, the normal flow of metabolites through the TCA cycle is disrupted, leading to the accumulation of succinate. According to the succinate accumulation hypothesis [18], mitochondrial succinate gains access to the cytosol and nucleus via metabolite transporters and acts as an oncometabolite [18, 19]. Because it is a byproduct in the conserved reaction mechanism of dozens of 2-oxoglutarate-dependent dioxygenases, accumulated succinate can act a competitive inhibitor of these enzymes, causing a wide variety of cellular impacts. These effects include inhibition of dioxygenases involved in the normal degradation of hypoxia-inducible factors (HIFs), and inhibition of demethylation of histones, DNA, and RNA [20]. There is also evidence for succinyl-CoA accumulation upon SDH loss in some contexts, driving post-translational lysine hypersuccinylation [20]. The resulting dysregulation of metabolism and epigenetics is tumorigenic in certain tissues [21].

Upon SDH loss, chromaffin and glomus cells of the paraganglia can give rise to PPGL [22]. The basis for this cell-specificity in PPGL tumorigenesis following SDH loss is unknown. Chromaffin cells are primarily found in the adrenal medulla and are responsible for the production and secretion of catecholamines such as adrenaline and noradrenaline [23]. Extra-adrenal paraganglia, which include glomus cells and other cell clusters derived from neural crest progenitors, also contribute to PPGL and can be found in various locations such as the head, neck, chest, abdomen, and pelvis [24, 25]. It remains unclear what cellular features unique to these tissues sustain viability and proliferation of SDH-loss cells during PPGL tumorigenesis. Insights may shed light on potential therapeutic interventions. Moreover, understanding PPGL tissue specificity is important in the quest for relevant preclinical models [26–28].

In a previous study by Kľučková et al., WT and SDHB-loss immortalized mouse chromaffin cell lines (imCCs) were compared to WT and SDHB-deficient non-chromaffin cells to discern possible metabolic differences [29]. We note that while the literature designation of imCCs implies chromaffin cell function, our characterization shows these cells to lack chromaffin morphology (e.g. secretory granules) or classic chromaffin cell markers by RNA expression profile. We thus consider the cells to be "immortalized adrenal medulla-derived cells" possibly representing precursors of mature chromaffin cells. Here we confirm and significantly extend these prior results by comparison of these previously studied wild type (WT) and SDHB-loss imCCs with our previously created SDHC-loss immortalized mouse embryonic fibroblasts (iMEFs). We characterize cell morphologies, cell cycles and replication times, gene expression, and detailed metabolism in normoxia and hypoxia. As previously suggested [29], we confirm that SDHB-deficient imCCs retain detectable Complex I function in the absence of Complex II and appear less dependent on glycolysis than SDH-loss fibroblasts. The metabolic resilience of SDHB-loss imCCs is particularly striking in hypoxia. These results suggest possible survival advantages for SDH-loss imCCs vs. other SDH-loss cells, possibly hinting toward similar survival mechanisms in PPGL tumors. Our detailed comparative characterization sets the stage for unbiased screens to seek vulnerabilities of SDH-loss chromaffin cells.

Materials and methods

Cell culture

Unless otherwise specified, cell culture was performed at 37 °C, 95% humidity in room air (21% O_2) with 5% CO_2. Culture media consisted of high-glucose DMEM (Gibco # 11965118) with GlutaMAX™ (Gibco #10566016), 10% heat-inactivated FBS (Gibco #10082147) and a 0.5 mg/mL final concentration of penicillin/streptomycin (Gibco #15140122). Additional supplements included 1 mM sodium pyruvate (Gibco #11140035), 10 mM HEPES buffer (Gibco #15630130) and nonessential amino acids [100 μM final concentration each of glycine, alanine, asparagine, aspartic acid, glutamic acid, proline, and

serine (Gibco #11140035)]. Cells were supplied with fresh media every other day and replated based on their doubling rate when 80–90% confluence was reached. Cells for analysis of dioxygenase inhibition by succinate and hypoxia Seahorse studies were grown in 10% and 5% room air, respectively. for hypoxia-inducible factor analysis, cultured cells were seeded 24 h prior to hypoxia treatment, then exposed to 21% (room air) or 10% O_2 in an incubator, or 1% O_2 in a sealed hypoxia chamber placed in a heated incubator for 24 h. All experiments were performed within 7 passages from the initial seeding of frozen stocks.

Original generation of SDH-loss imCCs and iMEFs

Wild type and *Sdhb*$^{-/-}$ imCC lines were originally generated at the Paris Cardiovascular Research Center (PARCC) as previously described [30]. Briefly, P1 (129S2/SvPas) ES cells were transfected through electroporation with a targeting vector that included *Sdhb* exon 2 surrounded by *LoxP* sites, along with a neomycin (*neo*) selection cassette bordered by *FRT* sites. Two positive embryonic stem clones were selected to be injected into C57BL/6J blastocysts and create chimeras for germline transmission. Male transmitters were bred into a Flipase-expressing background to allow excision of the *neo* cassette. Derived C57BL/6J-*Sdhb*$^{+/fl}$ mice were bred to generate *Sdhb*$^{fl/fl}$ animals, allowing isolation of mouse chromaffin cells (mCC) from the adrenal medullae of these *Sdhb*$^{fl/fl}$ mice following previously described methods [31]. Cells were maintained in a standard culture environment at 37°C with 5% CO_2, using Dulbecco's modified Eagle's medium with glutamine and high glucose (Gibco #10566016). The medium was supplemented with 10% fetal bovine serum (Gibco #10437028) and 1% penicillin-streptomycin (Gibco #15140122). Remaining quiescent for 6 months, some cultures spontaneously initiated cells growing as immortalized clusters (imCCs). These immortalized cells were isolated and subjected to infection with 10^7 plaque-forming units (pfu)/mL of an Ad-CMV-iCre adenovirus expressing Cre recombinase (Cell BioLabs #1045). Cloning by limited dilution yielded two *Sdhb*$^{-/-}$ imCC clones referenced as clone 6 and clone 8. *Sdhb*$^{-/-}$ and *Sdhb*$^{+/+}$ imCC lines were cultured in standard medium. PCR genotyping of *Sdhb* status was determined by PCR using LJM-6539 (5'-$C_2ATGC_2AGTA_2C_4AGA_2T_2G_2$-3') and LJM-6540 (5'-$GTC_3AC_2TCACTGTAG_2TCAC$-3') as primers.

Immortalized mouse embryonic fibroblasts (iMEFs) lines were isolated from mice harboring a *loxP* gene trap construct from Sanger Institute sandwiching exon 4 of *Sdhc* as previously reported [32, 33]. *Sdhc*$^{fl/fl}$ mice were introduced to the C57BL/6J-*R26M*$^{2rtTA/M2rtTA}$ background to create mice in which *Sdhc* rearrangement could be induced by doxycycline-dependent expression of Cre recombinase via a tet-inducible promoter. After inducing rearrangement of the *Sdhc* gene by doxycycline treatment of *Sdhc*$^{fl/fl}$ and *Sdhc*$^{+/fl}$ iMEF lines for 5 d, cells were diluted into DMEM (Gibco # 11965118) supplemented with 0.5 mg/mL penicillin/streptomycin antibiotics (Gibco #15140122), MEM NEAA [containing glycine, alanine, asparagine, aspartic acid, glutamic acid, proline, and serine at a concentration of 100 µM (Gibco #11140035)], sodium pyruvate [1 mM (Gibco #11140035)], and HEPES buffer [10 mM (Gibco #15630130)]. Cloning was achieved by limited dilution. Incubation was at 37°C for 2 weeks before screening for colonies. Recovered clones were then expanded gradually from 12-well plates to T25 flasks in growth medium of the same composition. A small number of cells from each clone underwent DNA extraction and PCR analysis to determine the *Sdhc* gene rearrangement status. Clones exhibiting homogeneous *Sdhc* rearrangement were selected for expansion and establishing stocks of *Sdhc*$^{+/-}$ and *Sdhc*$^{-/-}$ iMEFs. Genotyping for CRE-recombined *Sdhc* product was carried using LJM-4429 (5'-$CT_2AGA_2CTGATC_4TGC_3$-3') and LJM-5125 (5'- $C_2TG_2A_2CTAGA_2T_2AT_2GATG_2ATG$-3').

Western blot analysis

Western blotting was used to confirm the loss of SDHB and SDHC proteins in imCCs and iMEFs, respectively. Cell pellets from all four lines (3 million cells each) were lysed in 150 µL cold RIPA buffer containing protease and phosphatase inhibitor cocktail (Santa Cruz Biotechnology # sc-24948). Sample lysates were then incubated on ice for 30 min with gentle vortex mixing every 10 min. Following centrifugation at 15,000×g for 15 min, protein quantification was carried out using a BCA protein assay kit (Pierce #A55864). Samples were heated to 70 °C for 10 min after the addition of reducing agent and an appropriate volume of 4× LDS denaturation buffer (Invitrogen #NP0007). Denatured samples (35 µg) were subjected to electrophoresis through NuPAGE 10% Bis-Tris protein gels (Invitrogen #NP0315BOX) in MES-SDS running buffer (Invitrogen #NP0002) at 150 V for 1 h. PVDF membrane transfer was performed according to the manufacturer's protocol in a Novex Western Transfer Apparatus in NuPAGE transfer buffer containing 20% methanol. The transferring process was at 4 °C (30 V, 245 mA) for 90 min. The quality of transfer was confirmed by Ponceau S staining. Membranes were then blocked with 3% non-fat milk for 1 h at room temperature, followed by three 5-min washes in TBST buffer. All antibodies were purchased from Abcam, and antibody combinations were tested to confirm lack of cross-reactivity. A dilution buffer was prepared using 7.5 mL TBST, 2.5 mL 4% BSA, and 250 µL 0.5% sodium azide. Antibody against and PCNA (Abcam #ab29, 1:10,000) was used as

loading control. Anti-SDHB (Abcam #ab175225, 1:5000) and anti-SDHC (Abcam #ab155999, 1:1000) antibodies were used to detect their protein targets at 32 kDa and 19 kDa, respectively. After 48 h of incubation at 4 °C, blots were washed three times in TBST before staining with IRDye® 680rd goat anti-rabbit IgG (LI-COR #926-68071, 1:15,000) or 800cw goat anti-mouse IgG secondary antibody (LI-COR #926-32210, 1:15,000) antibodies in TBST with 3% non-fat milk for 1 h at room temperature prior to imaging with Amersham Typhoon 5 Biomolecular Imager (Amersham Typhoon, Uppsala, Sweden).

For immunoblotting analysis of HIF1/2α, DNA damage and mitochondrial complexes, cultured cells were harvested by washing with ice cold PBS, dissociated with ice cold trypsin-EDTA (Gibco 25300054), and neutralized with ice cold culture media. Cells were pelleted at 700×g and washed with ice cold PBS. Total cellular protein was extracted on ice using RIPA lysis buffer (ChemCruz sc-24948) with additional phosphatase inhibitors (ThermoFisher #78420) and soluble protein lysate was isolated after clarifying the extract at 15,000×g. Quantification of total soluble protein concentration was performed using the BCA protein assay according to the manufacturer's protocol (Pierce #23225). Protein lysates were denatured and reduced in reducing agent (Invitrogen #NP0004) and LDS buffer (Invitrogen #NP0007) at 95°C for 5 min immediately after samples protein levels were quantified and again prior to gel loading. Lysate (45 µg protein per sample) was loaded on 4–12% Bis-Tris gels (Invitrogen #NP0335BOX) and subjected to SDS-PAGE in reducing MES or MOPS buffer (Invitrogen #NP0002, NP0001 and NP0005). Proteins were then transferred to a PVDF membrane (Bio-Rad #1620174) in transfer buffer (Invitrogen #NP00061) containing either 10% methanol and 0.01% SDS for HIF1α and HIF2α detection, or 20% methanol for all other proteins. The membrane was then briefly stained with Ponceau S, imaged on a Typhoon 5 biomolecular imager (Amersham Typhoon, Uppsala, Sweden), destained with deionized water, and blocked in 5% non-fat dairy milk dissolved in TBST for 1–2 h at room temperature. The membrane was washed with TBST before incubating in primary antibodies diluted into 5% BSA dissolved in TBST overnight with gentle rocking at 4°C overnight. The membrane was then washed with TBST prior to incubation with fluorescent secondary antibodies (LI-COR, IRDye 680RD goat anti-rabbit #926-68071, 1:20,000 and IRDye 800CW goat anti-mouse #926-32210, 1:20,000) with gentle rocking for 15–20 min at room temperature. The membrane was washed with TBST, then with TBS prior to imaging on the Typhoon 5. Primary antibodies used were nti-HIF1α (Cayman Chemical rabbit polyclonal 10006421; 1:1000), anti-HIF2α (Novus Biologicals mouse monoclonal NB100-132; 1:500), anti-α-tubulin (abcam mouse monoclonal ab7291; 1:50,000), anti-H3 (abcam mouse monoclonal ab10799; 1:1000), anti-H3K9me3 (Active Motif rabbit polyclonal 39162; 1:5000), Anti-H2A.X (Active Motif rabbit polyclonal 39690; 1:2000), anti-γH2A.X (phospho S139) (Millipore-Sigma mouse monoclonal 05-636; 1:1000), anti-COX10 (CST #24744, 1:1000), anti-NDUFS1 (CST 70264, 1:1000) and anti-cytochrome c (CST 11940, 1:1000).

Histone isolation

Cultured cells were harvested by washing with ice cold PBS, dissociated with ice cold trypsin-EDTA (Gibco 25300054), and neutralized with ice cold culture media. Cells were pelleted at 700×g and washed with ice cold PBS. Nuclei were extracted by lysing cells at 4 °C in TEB (PBS containing 0.5% Triton X-100 and protease inhibitor cocktail) for 10 min with gentle agitation, then pelleted at 2000×g at 4 °C. Pelleted nuclei were washed twice with TEB by centrifugation at 1500×g. Nuclei pellets were frozen at -20°C for later histone extraction. Histones were obtained by acid extraction for 1 h with 0.4 N H_2SO_4 and clarified at 15,000×g at 4°C. Histones were then precipitated from the supernatant with 100% TCA to achieve a final TCA concentration of 33% v/v and incubated on ice for 30 min. Histones were pelleted at 15,000×g at 4°C, washed twice with ice cold acetone by centrifugation 15,000×g at 4°C to remove the acid. Histone pellets were air dried and stored at -80°C until use. Histone pellets were then resuspended in ultrapure H_2O and quantified using A_{230} measurement, with final concentration being estimated using the formula:

$$histone\,mass\,(mg/mL) = A_{230}/0.42. \quad (1)$$

Cell measurements

Cells were grown to 20–90% confluence in 6-well plates. Harvest was accomplished by incubating cells in 0.5 mL of 0.25% trypsin (Gibco #25200056) for 5 min (control lines) or 8 min (SDH-loss lines) with addition of light mechanical dissociation before trypsin quenching by addition of 1 mL media and viewing under a microscope. Average cell diameter was obtained by dividing the known diameter of a saturated field of view by the number of contained cells. Results were validated using a Countess II FL Automated Cell Counter instrument (Invitrogen, Carlsbad, CA). Doubling time for imCCs and iMEFs lines was obtained using an adaptation of a previously described method [32], replacing manual imaging with IncuCyte® technology (Sartorius, Ann Arbor, MI, USA) according to the manufacturer's protocol. In short, cells were seeded at a low density and incubated in the IncuCyte instrument for 5 d, supplied with fresh media every 2 d. Proliferation was determined using a label-free count method where phase objects were counted

2 h before the cultures reached confluence (defined as a cell density when the analysis software fails to distinguish individual phase objects). Doubling time (T_d) was calculated based on cell counts n_1 and n_2 at times t_1 and t_2, respectively, according to:

$$T_d = (t_2 - t_1)\left[\frac{\log 2}{\log\left(\frac{n_2}{n_1}\right)}\right] \quad (2)$$

Trypsin sensitivity

Three replicates of five million cells for each of the four lines were seeded in T-75 flasks and allowed to plate overnight prior to trypsinization assay. The following morning, cells were incubated with 5 mL of 0.25% trypsin (Gibco #25200056) for 5 min and then quenched with a 4× volume of growth media. The number of detached cells was determined by hemocytometer based on a sample of the supernatant. For each line, a counting control was used to calculate the final number of cells. This counting control involved trypsinization prolonged for 10 min with light mechanical shaking to calculate the total number of cells.

Cell cycle analysis

Three replicates of two million cells per sample for each of the four cell lines were harvested by aspirating culture medium followed by three washes in PBS. Cells were then fixed and permeabilized in ice cold 70% ethanol for 3 days in -20° C. On day 4, samples underwent 3 additional washes followed by resuspension in 1 mL PBS in flow tubes (1 million cells per mL). One drop Propidium Iodide Ready Flow™ Reagent (Invitrogen #R37169) per million cells was added with incubation in the dark for 45 min before sample analysis on a BD FACSymphony A3 Flow Cytometer at 50,000 cells per sample (Becton, Dickinson and Co, Vernon Hills, IL, USA). For Live cell cycle analysis, 3 replicate T-175 flasks per line were harvested at 80% confluency by 0.25% Trypsin (Gibco #25200056). The cells were then washed and suspended in PBS. One million cells were counted and diluted in a total of 1 mL PBS. Live cell staining was done using Hoechst 33,342 Ready Flow™ Reagent [(Invitrogen #R37165); 2 drops per 1 million cells] and the samples were incubated in 37 C for 60 min prior to cell sorting. Data analysis was performed using the univariate cell cycle model in FlowJo™ v10.10 (FlowJo, LLC, Ashland, OR, USA).

Metabolite quantitation

imCCs and iMEFs were grown to ~80–90% confluence (~1 million cells 100-cm dish). Cells were washed three times with PBS to remove media. Cells were frozen on dry ice and 1.5 mL chilled methanol (-20 °C) was added to each dish. Cells were then scraped into methanol using a sterile plastic scraper with a rubber head. The resulting slurries were transferred to 2-mL conical tubes and frozen on dry ice. Samples were stored at -80 °C prior to analysis. TCA cycle-related analytes were measured by gas chromatography/mass spectrometry (GC/MS) with technical assistance from the Mayo Clinic Metabolomics Core facility as previously described [34, 35].

Electron microscopy

Sample processing for electron microscopy was performed in the Mayo Clinic Microscopy and Cell Analysis Core. One million control or SDH-loss imCCs or iMEFs (4 samples total) were washed twice in PBS and fixed in 5 mL McDowell Trump's fixative (Electron Microscopy Sciences # 18030-05) using gentle vortex mixing. Micrographs were acquired using a JEOL 1400 Plus transmission electron microscope (JEOL, Inc., Peabody, MA) at 80 kV equipped with a Gatan Orius camera (Gatan, Inc., Warrendale, PA) [36].

F-actin staining

F-actin staining was performed using ActinGreen Alexa-Fluor™ 488 phalloidin (Invitrogen # R37110) according to the manufacturer's protocol. Briefly, 10,000–20,000 cells were seeded on glass-bottom plates and allowed to adhere overnight. Cells were then washed with PBS and fixed in 4% formaldehyde (Sigma Aldrich #1039991000) in PBS solution for 15 min followed by permeabilization in 0.1% Triton-X100 (Sigma Aldrich #X100-100ML) for 10 min. After an additional wash in PBS, cells were incubated with 1 μg/mL DAPI for 5 min followed by addition of 1 drop ActinGreen for 30 min. Cells were then imaged using Olympus BX50 DIC Fluorescence Microscope (Olympus Corporation of the Americas, Center Valley, PA, USA) and processed using ZEISS TIVATO 700 (ZEISS White Plains, NY, US).

Chromosome counting by fluorescence in situ hybridization (FISH)

FISH for determination of total mouse chromosome number was performed in the Genomics Culture Laboratory of the Mayo Clinic Division of Laboratory Genetics and Genomics. Counting and analysis was performed with the IKAROS and ISIS digital FISH imaging system (MetaSystems, Altlussheim, Germany).

Cell labeling and confocal imaging

imCCs and iMEFs were plated at a density of ~10,000 cells/well into 8-well Ibidi μ-slide plates (Ibidi #80826) and allowed to adhere. Cells were treated for 15 min with growth medium (37˚C) containing 100 nM MitoTracker® Green FM (Invitrogen #M46750; excitation/emission wavelength 490/516 nm) followed by washing

with Hanks' Balanced Salt Solution [HBSS (Invitrogen #11575032)]. Cells were imaged by confocal microscopy using instrumentation previously described [37–41]. The dynamic range for imaging was set by first scanning a region containing no fluorescence signal and then a second region of interest containing maximum fluorescence. A series of 0.5 µm thick optical slices were acquired for each cell. This Z-stack was acquired and analyzed using NIS-Elements software (Nikon Instruments Inc., Melville, NY).

Estimation of mitochondrial volume density

Three-dimensional reconstructions were obtained and deconvolved using the algorithm available in NIS-Elements analysis software (Modified Richardson Lucy method; Point Scan Confocal modality; Nikon Instruments Inc.) [38, 40–42]. Deconvolution was applied to the image signal-to-noise ratio so as to improve contrast and edge detection. Voxel dimensions of each deconvolved optical slice were 0.207×0.207×0.5 µm. Cell boundaries were then delineated using ImageJ-Fiji 2.16.0 software (https://imagej.nih.gov/ij/). Using the mitochon drial analyzer module of ImageJ software, Z-stacks were then processed for background correction and ridge filter detection [39, 40, 43–45]. Mitochondria were identified by thresholding to create a binary image and then skeletonized for morphometric analysis. Using thresholded images, total mitochondrial volume was measured using the mitochondrial analyzer software module, where the number of voxels containing fluorescently labeled mitochondria within a single delineated cell was determined [39, 46]. Mitochondrial volume density was calculated as the ratio of mitochondrial volume within the cell to the total volume of the delineated cell [40–42, 47–49].

Quantitative histochemical estimation of SDH reaction velocity

Images were acquired using a Nikon Eclipse A1 laser scanning confocal microscope (RRID: SCR_020317) with a 60×/1.4 NA oil-immersion objective at 12-bit resolution into a 1,024×1,024-pixel array using the transmitted light channel was used for image acquisition. An interference filter with a peak emission wavelength of 570 nm was placed in the light path to limit the spectral range of the light source to the maximum absorption wavelength of $NBT_{dfz[36]}$. The measured gray level (GL) of the microscope was calibrated to known optical density (OD) units using a photographic density stepwedge tablet (0.04–2.20 OD units in increments of 0.15 OD; Stouffer Industries, Mishawaka, IN). The dynamic range of the microscope was adjusted to take advantage of the full range of OD while avoiding saturation of the images at both ends of the OD range [50]. The quantitative histochemical procedure for measuring SDH reaction velocity was then performed. This technique has been previously described in detail for single skeletal muscle fibers [38–47, 51] and airway smooth muscle cells [50, 52–54]. imCCs and iMEFs were plated in 8-well Ibidi µ-slide plates (Ibidi #80826) at a density of ~10,000 cells/well and incubated to allow for cell adherence. Cells were exposed to solutions containing 1.5 mM nitro blue tetrazolium (NBT; reaction indicator), 5 mM EDTA, 1 mM mPMS, and 0.75 mM sodium azide in 0.1 M phosphate buffer (pH: 7.4). In a separate series of experiments, the dependence of the SDH reaction on succinate concentration was assessed, and a concentration of 80 mM succinate was found to produce the maximum velocity of the SDH reaction in both imCCs and iMEFs. In the quantitative histochemical procedure, the progressive precipitation of colored NBT_{dfz} due to the reduction of NBT is used as the reaction indicator. Experiments were performed at room temperature (22±1 °C), with similar parameters maintained across preparations. A series of 0.5 µm thick optical slices was acquired every 15 s across a 10-min period. The Z-stack was acquired and analyzed using NIS-Elements software (version 5.20.02; RRID: SCR_014329; Nikon Instruments Inc., Melville, NY). From the optical slices, the cells were delineated as the region of interest while the nuclei were excluded. NBT_{dfz} precipitation was measured as the progressive increase in OD as the SDH reaction proceeded. The change in average OD within the selected region of interest was measured every 15 s across a 10-min period. The SDH_{max} was then determined using the Beer-Lambert equation:

$$SDH_{max} = \frac{d\,[NBT_{dfz}]}{dt} = \frac{dOD/dT}{kl} \tag{3}$$

Where OD is measured based on the calibrated gray level of NBT_{dfz} accumulation, k is the molar extinction coefficient for NBT_{dfz} (26,478 M^{-1} cm^{-1}), and l is the pathlength for light absorbance (0.5 µm optical slice thickness). SDH_{max} is expressed as mmol fumarate per liter of cell per min.

Multiple cells were visualized within a single microscopic field and the cells whose borders were not overlapping were analyzed. Typically, this selection process resulted in analyzing 3 to 4 cells per field.

Oxygen consumption rate (OCR)

imCCs and iMEFs were plated into Seahorse XFe96 cell culture microplates (Agilent Technologies # 204626-100) at three densities (30,000, 60,000 and 100,000 cells per well) to establish optimal signal-to-noise ratios. Because of the larger size of plated SDH-loss imCCs, an equal number of cells occupy more surface area and grow more slowly at high confluence. Thus, higher cell numbers are impractical. Wells were allowed to recover overnight.

OCR was measured by the mitochondrial stress test assay performed using the Seahorse XFe96 Bioanalyzer (Agilent Technologies, Santa Clara, CA, USA) according to the manufacturer's instructions and as described previously [55]. Prior to the assay, growth media were replaced with Seahorse assay medium consisting of Seahorse XF DMEM base medium (Agilent #103335-100) supplemented with 17.5 mM glucose (Gibco #A2494001), 1 mM sodium pyruvate (Gibco #11360070), and 2 mM glutamine (Gibco #25030081) at pH 7.4, and incubated for 1 h in a non-CO_2 incubator. Optimal concentration of inhibitors and FCCP used for both cells were found to be: 1 µM oligomycin (ATP uncoupler), 1 µM FCCP (accelerates electron transport chain), and 0.5 µM antimycin A (Complex III inhibitor) with 1 µM rotenone (Complex I inhibitor). OCR measurements were normalized to total adherent cell count, assessed using 1 µg/mL Hoechst 33,342 Solution (Invitrogen #H3570; excitation/emission wavelength: 361/486 nm) and using the Seahorse XF Imaging and Normalization on a Cytation 1 (BioTek, Winooski, VT).

For physiologic O_2 studies, imCCs and iMEFs were adapted for three passages in 5% O_2/5% CO_2 using a Biospherix XVivo X3 incubator (Biospherix, Parish, NY) with media conditioned to 5% O_2/5% CO_2 with a Hypoxycool media conditioner (Baker, Sanford, ME). Following adaptation, cells were plated, and Seahorse assays performed as above with modifications. To enable O_2 control, the Seahorse XFe96 was housed in Hypoxia Glove Box (Coy Laboratory Products, Grass Lake, MI) and stabilized to 5% O_2/0% CO_2 for 24 h prior to the assay and Seahorse XF media was conditioned to 5% O_2/0% CO_2. Cells were not seeded into the final column of the XFe96 cell culture plate allowing these wells to serve as 0% O_2 control wells. Following replacement of growth media with Seahorse XF media (or calibrant in 0% O_2 control wells), cells were incubated in Seahorse XFe96 for 1 h to allow for degassing of CO_2. The Seahorse XFe96 was operated in Hypoxia Mode and injection ports for 0% O_2 control wells were loaded with 1 M sodium sulfite.

Electron transport chain complex-specific Seahorse extracellular flux analysis was performed as previously described [55]. In brief, imCCs and iMEFs were plated into Seahorse XFe96 cell culture microplates (Agilent # 204626-100). Prior to the assay, growth media was replaced with Mitochondrial Assay Solution (MAS, pH 7.4 at 37 C, 220 mM mannitol, 70 mM sucrose, 10 mM KH_2PO_4, 5 mM $MgCl_2$, 2 mM HEPES, 1 mM EGTA and 0.2% (w/v) fatty-acid free BSA, 1 mM malate, 10 mM pyruvate, 4 mM ADP, 1 nM XF Plasma Membrane Permeabilization (PMP) agent and 4 µM FCCP. Sequential injection of complex specific substrates and inhibitors allow the quantitation of complex activity, baseline (complex I activity), 2 µM rotenone (inhibit Complex I), 10 mM succinate (complex II), and 2 µM Antimycin A (inhibit Complex III downstream of Complex I and II).

RNA sequencing

Cell pellets from imCCs and iMEFs were collected from three replicates at 24, 48 and 72 h after seeding. RNA was extracted using RNeasy kits (Qiagen #74104) and DNA removed by addition of on-column DNase I treatment (Thermo Scientific #EN0521). Further RNA purification and concentration were performed using Concentrator-5 (Zymo #R1013) prior to analysis in the Mayo Clinic Medical Genome Facility where indexed deep sequencing libraries were prepared using the Illumina TruSeq mRNA v2 kit (Illumina #RS-122-2001). Deep sequencing was conducted on a NextSeq P2 flow cell (Illumina, San Diego, CA, USA) for an approximate total of 70 M reads/sample. For analysis, paired-end sequence reads were aligned to the mm9 mouse reference genome using the STAR fast read aligner [56]. Gene level counts were obtained using featureCounts v1.4.6 from the subRead package [57]. Differential expression analysis was performed with DESeq2 [58]. RStudio, Bioconductor 3.17 and R packages: ggplot2; Complex heatmap [59] were used for analysis and plotting.

Statistical analyses

Relevant statistical tests are described in individual figure legends.

Results

Phenotypic changes following SDH loss in imCCs and iMEFs

SDH loss influences cellular biochemistry, metabolism, gene expression and morphology, particularly due to succinate accumulation [60–62]. Our goal was to compare and contrast SDH loss effects in two different available cell models: WT vs. SDHB-loss imCCs and heterozygous vs. SDHC-loss iMEFs. SDH-loss lines were confirmed by genotyping (Supplemental Fig. S1A-D). Western blotting for SDHB and SDHC indicated that target gene knockout results in complete loss of the targeted SDH subunit with detectable traces of residual the non-targeted SDH subunit (Supplemental Fig. S2A). This confirms that disrupted SDH complex assembly destabilizes SDHB/C subunits [63]. Similarly, mitochondrial complex western blotting assessment of COX10, NDUFS1 (oxidoreductase core of Complex I) and cytochrome c suggest SDH loss affects other components of the Respiratory Chain beyond SDH inhibition (Supplemental Fig. S2B). Furthermore, RNAseq analysis involving mitochondrial fission and fusion markers showed differential expression in SDH-loss cells compared to their respective controls, most notably in imCCs. Certain genes like *Mfn1*, *Mfn2*,

and *Opa1* show more subtle changes in iMEFs compared to imCCs, suggesting greater effect on fusion genes more in imCCs. By contrast, there appears to be a stronger bias toward mitochondrial fission in SDH-loss iMEFs, as evidenced by robust upregulation of Fis1 and Drp1 (Supplemental Fig. S2C). We confirmed loss of SDH enzyme activity in SDH-loss lines vs. control lines using an imaging-based SDH activity assay (Fig. 1A). It is unknown if residual SDH activity in *Sdhc*$^{-/-}$ iMEFs could be attributable to residual SDHB protein (Supplemental Fig. S2A) that might remain associated with membrane unbound SDHA catalytic subunit that, if properly flavinylated, might confer a trace of enzymatic function [64].

Not surprisingly, SDH loss dramatically slows the proliferation rate of both iMEFs and imCCs, presumably due to reduced ATP production and TCA cycle truncation and derangement as described for other models of SDH-loss [65, 66]. Cell doubling time was increased more (~4-fold) for imCCs, compared to SDHC-loss iMEFs (~2-fold) (Fig. 1B). As previously noted for SDH-loss imCC lines [29], cell diameter was 35% larger in suspension. Cell enlargement was observed to a lesser extent in *Sdhc*$^{-/-}$ iMEFs (Fig. 1C and Supplemental Fig. S3). This phenotype is also confirmed through flow cytometry forward scatter (FSC) and side scatter (SSC) signatures of SDH-loss cells compared to controls (Supplemental Fig. S3A), and is reflected as well in their adherent state

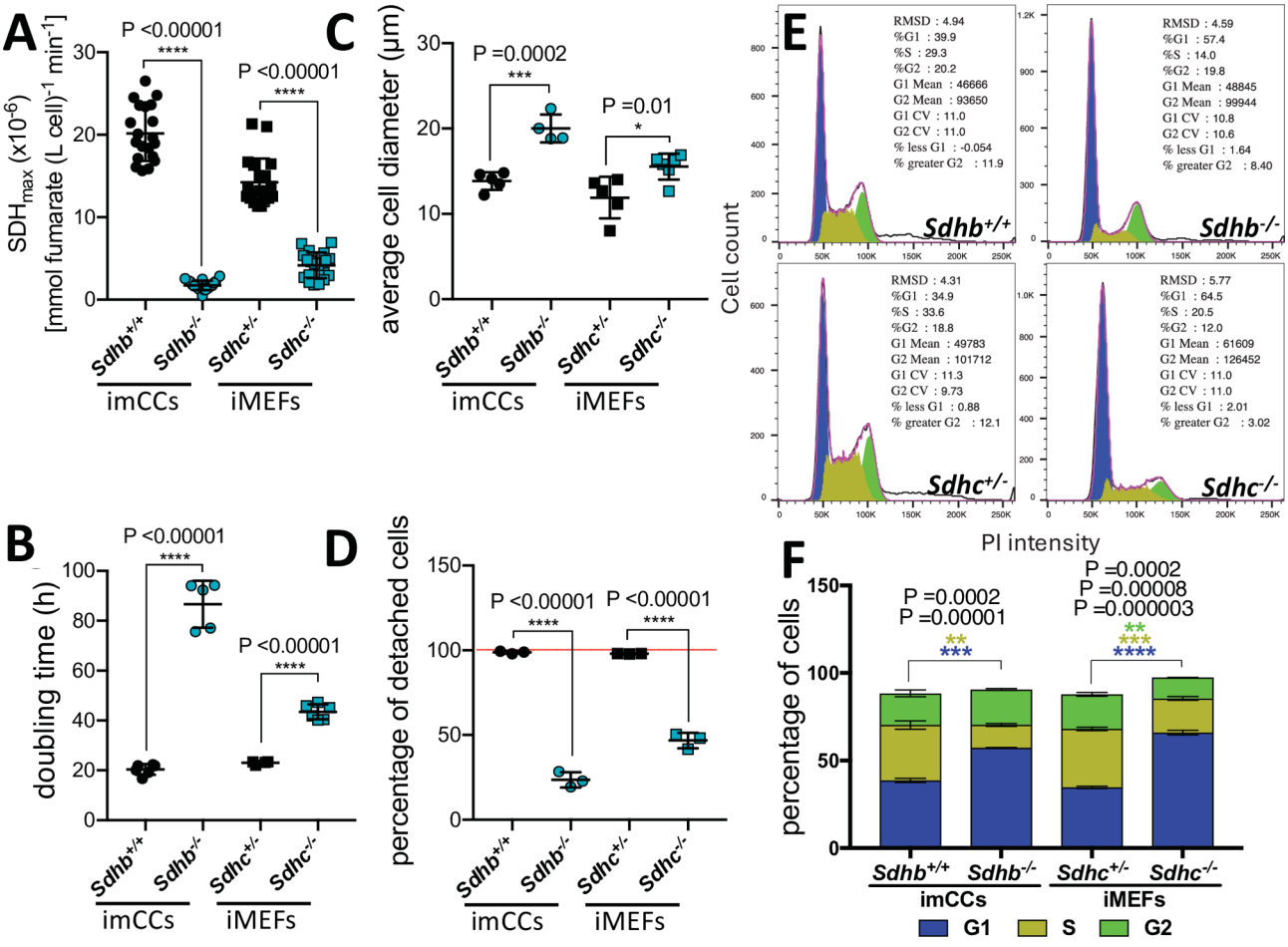

Fig. 1 SDH-deficiency induces phenotypic changes in imCCs and iMEFs. (**A**) Maximum velocity of SDH catalysis (SDH_{max}) calculated according to Eq. 3 ($n = 20$ cells per line). (**B**) Quantitation of cell doubling time based on Eq. 2 for imCCs and iMEFs ($n = 6$ wells per line). (**C**) Average cell diameter for control and SDH-loss imCCs and iMEFs. Data represent average calculated diameter for 6 fields per line. (**D**) Percentage of detached cells following trypsinization for 5 min compared to a counting control treated with excess trypsin and mechanical force for total detachment (100%, indicated by red line). *P*-values are calculated using student's t-test and the number of asterisks indicates degree of significance. (**E**) Examples of Flowjo-generated cell cycle analysis histograms showing percentage of the indicated cells in each of the indicated cell cycle phases (G1, S or G2) based on DNA content (measured by fluorescence intensity) using a Watson analysis model ($n = 50{,}000$ cells per sample). (**F**) average percentage of cells in each of the indicated cell cycle phases (G1, S or G2) for each control or SDH-loss line shown as mean ± SEM ($n = 3$ samples per line processed in a single run). RMSD values for the depicted histograms are *Sdhb*$^{+/+}$imCCs: 4.94; *Sdhb*$^{-/-}$imCCs: 4.59; *Sdhc*$^{+/-}$iMEFs: 4.31 and *Sdhc*$^{-/-}$iMEFs: 5.77. These values are representative of the replicate samples. Totals do not all reach 100% because of the presence of cells with DNA content not assigned to any of the indicated phases. *P*-values are calculated using Bonferroni correction for multiple t-tests and the number of asterisks indicates degree of significance

(Supplemental Fig. S3B) Interestingly, SDH-loss cells showed increased intercellular and surface adherence as judged by higher resistance to trypsinization (Fig. 1D).

In light of the extended cell replication time, cell cycle analysis was performed on fixed cells using Propidium Iodide (PI). Results are shown in Fig. 1E-F. These data reveal cell-type specific cell cycle effects of SDH loss. *Sdhb*$^{-/-}$ imCCs show a prolonged G1 phase and abbreviated S phase, possibly indicating changes in DNA repair pathways [67]. Similar results were seen in *Sdhc*$^{-/-}$ iMEFs, in addition to a prolonged G2 phase (Fig. 1E-F), often taken as evidence of DNA damage. However, Western blotting results probing against the canonical γH2AX DNA damage marker did not demonstrate a significant constitutive DNA damage response in SDH-loss iMEFs (Supplemental Fig. S4C) though some previous evidence of such an effect has been reported [68]. Live cell analysis using Hoechst dye was also performed with varying reproducibility compared to fixed cell analysis due to different levels of PBS tolerance impacting WT lines (Supplemental Figs. S4A-B). While neither dye can reliably compare signal intensity across different cell types, data in Fig. 1E and Supplemental Fig. S4A demonstrate differences in total DNA content for SDH-loss lines vs. their respective controls, as validated below.

Consequences of succinate accumulation on TCA metabolites and dioxygenases

A unique signature of SDH-loss PPGL tumors is the accumulation of succinate both inside and outside of the mitochondrial matrix. Succinate accumulation is associated with an aggressive tumor phenotype and poor clinical outcomes [15, 69]. To investigate the effect of SDH deletion on succinate and other metabolites, a mass spectrometry-based quantitative metabolomic analysis was completed (Fig. 2A-C). The results indicate a striking ~ *130-fold increase in cellular succinate levels* for both *Sdhb*$^{-/-}$ imCCs and *Sdhc*$^{-/-}$ iMEFs. Moreover, SDH-loss cells demonstrate a general trend in decreased levels of other TCA-related metabolites, particularly for SDHB-loss imCCs when normalized to cellular protein (Fig. 2B). The exception is that SDH-loss iMEFs preserve approximately normal levels of isocitrate, 2-hydroxyglutarate and glutamate. Importantly, SDH-loss iMEFs accumulate lactate, while SDH-loss imCCs do not. This suggests a greater reliance of SDH-loss iMEFs on glycolysis and lactate dehydrogenase activity for NAD^+ regeneration. *This result points to the surprising conclusion that SDH-loss imCCs maintain a degree of fitness without a Warburg-like shift to glycolysis* [70]. It is noteworthy that normalizing TCA metabolites to cell counts suggests that most

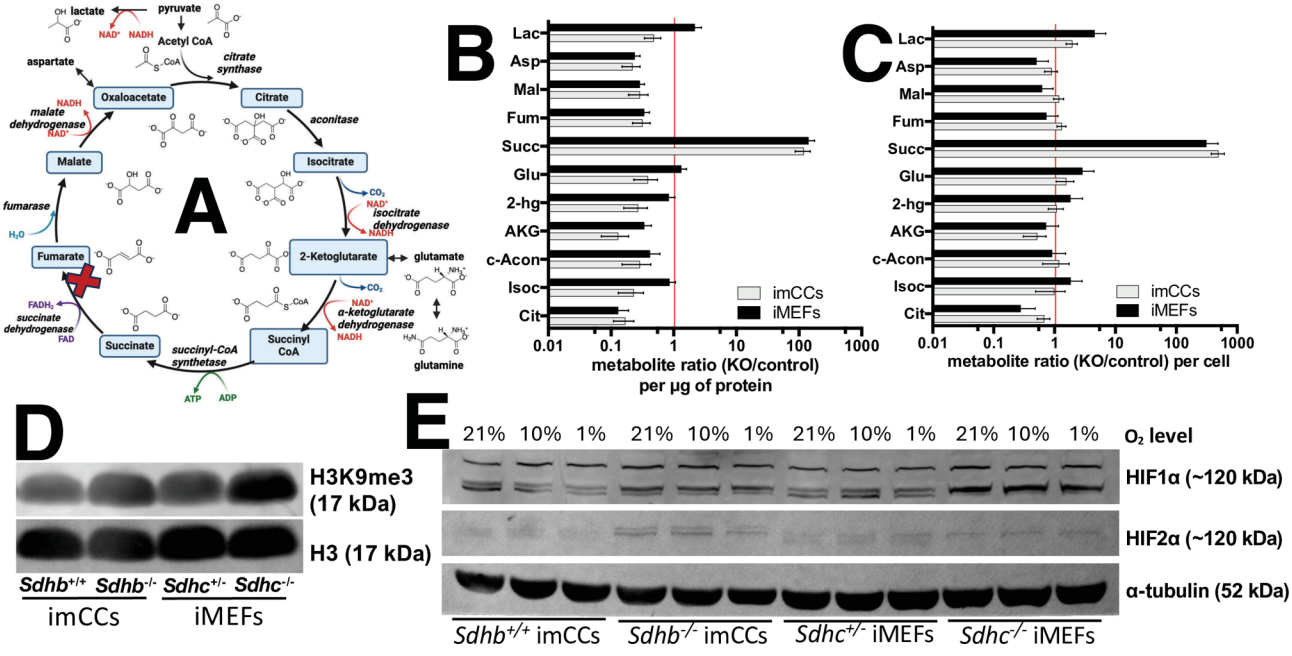

Fig. 2 Metabolite profiling and effects on DNA methylation. (**A**) Schematic overview of TCA cycle highlighting the loss of SDH function (red "X"). (**B-C**) Relative metabolite levels (log scale) in SDH-loss cells compared to their respective controls ($n = 3$ samples of million cells per line, data shown as mean ± SEM) normalized to protein content (**B**) or per cell (**C**). Cell normalization data were accounted for mathematically by calculating the number of cells in each sample using a standard curve for protein content per 1 M cells. Lac: lactate; Asp: aspartate; Mal: malate; Fum: fumarate; Succ: succinate; Glu: glucose; 2-hg, 2-hydroxyglutarate; AKG, 2-oxoglutarate; c-Acon: cis-aconitate; Isoc: isocitrate; Cit: citrate. (**D**) Western blot of H3K9me3, detected at 17 kDa, where hypermethylation serves as a marker of succinate inhibition of JMJD demethylases, a subfamily of OG-dependent dioxygenases. Anti-histone H3 is used as loading control, also detected at 17 kDa. (**E**) Western Blot analysis for HIF1/2α levels in various indicated oxygen concentrations. Protein extracts from the indicated cell lines were probed with anti-HIF1α or HIF2α, both detected at 120 kDa (two upper panels). α-tubulin was used as a loading control and detected at 50 kDa (lower panel)

metabolites (except succinate) remain close to WT levels, implying that the metabolic activity per cell is similar, despite the increase in protein content. Overall, these results suggest that SDH-loss lines have lower metabolic activity per unit of protein per cell.

As posited by the succinate accumulation hypothesis [19], succinate accumulation associated with SDH loss has implications for the function of 2-oxoglutarate (2-OG)-dependent dioxygenases where elevated succinate can cause enzyme competitive inhibition [71]. This is especially true for JMJD demethylases, which rely on 2-OG as a co-substrate to catalyze the removal of methyl groups from histones, a process critical for epigenetic regulation. High levels of succinate can disrupt this process, leading to accumulation of methylated histone residues in chromatin. Histone hypermethylation thus serves as an indicator of succinate inhibition. We confirmed this for both control and SDH-loss imCCs and iMEFs by monitoring H3K9me3 using western blotting (Fig. 2D). We also monitored levels of Hypoxia-Inducible Factor 1α and 2α by western blotting (Fig. 2E). These experiments were performed in various oxygen conditions according to reported methods and previously published reports [27, 72] Interestingly, oxygen concentration did not detectable increase HIF1α stabilization in WT or SDH-loss cells. Rather, SDH-loss cells appear to accumulate higher amounts of HIF1α isoforms with higher molecular weight (suggesting post-translational modifications) than the same proteins detected in control cells. Also unexpectedly, reduced oxygen concentration did not increase HIF2α stabilization. Again, SDH-loss cells demonstrate higher amounts of larger isoforms consistent with post-translational modification than HIF2α isolated from control cells, as noted by the the shift to increasing size in the double-band HIF2α pattern for SDH-loss imCC vs. control cells, and the predominance of the upper band of the doublet in SDH-loss iMEFs vs. control cells (Fig. 2E). These results confirm succinate inhibition of histone demethylases in SDH-loss cells, but reveal more complex effects on HIF proteins.

Morphological changes induced by SDH loss

Due to its key role in both the mitochondrial TCA cycle and mitochondrial electron transport chain, we predicted that the loss of SDH function would alter mitochondrial morphology [73, 74]. To test this hypothesis, we utilized electron microscopy for ultrastructural characterization of control and SDH-loss imCCs and iMEFs. Our results confirmed striking SDH-loss pathology in both imCCs and iMEFs, most impressively in the former (Fig. 3A and Supplemental Fig. S5A). SDH-loss imCCs exhibit dramatically enlarged, 'ghostly' mitochondria identifiable by faint residual internal cristae, and often characterized by a single electron-dense central condensate (Fig. 3A,

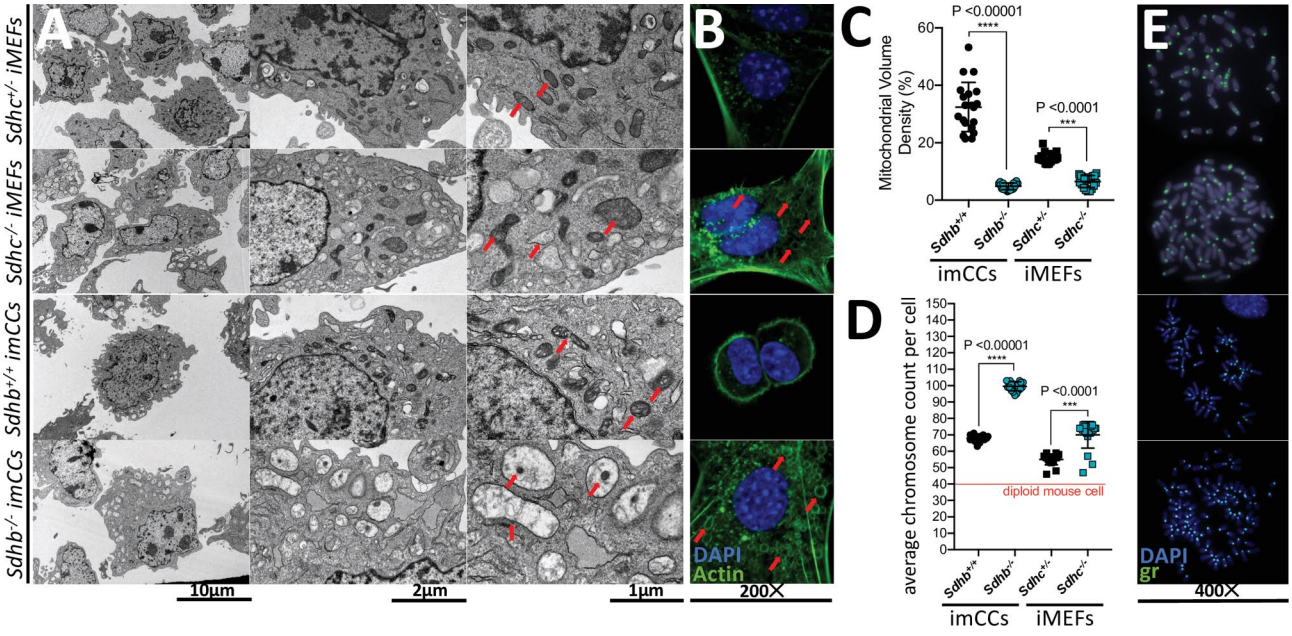

Fig. 3 Altered mitochondrial and cellular morphology following SDH loss. (**A**) Representative electron micrographs of mitochondria for the indicated cell lines at the indicated magnifications. Individual examples of mitochondria are indicated by red arrows in the far-right panels. (**B**) Staining of the same cell lines to show unusual circumferential F-actin staining (red arrows) around enlarged mitochondria in SDH-loss cells. (**C**) Mitochondrial volume density measurement by 3D microscopy for the four indicated lines ($n = 20$ cells per line). (**D**) Average chromosome counts per cell for each control and SDH-loss line ($n = 20$ cells per line). Red line symbolizes the normal chromosomal count of a diploid mouse cell. Error bars in panels C-D indicate mean ± SD. *P*-values are calculated using student's t-test for each experimental and control pair and the number of asterisks indicate degree of significance. (**E**) Micrographs of single-cell FISH analysis with a mouse pan centromere probe (green) to mark the centromeres on DAPI stained chromosomes

bottom right). Some of these features were also observed in SDH-loss iMEFs, though more mitochondria appeared to maintain structural integrity, resulting in more diverse mitochondrial morphology in SDH-loss iMEFs. We observed an unusual pattern of F-actin surrounding enlarged SDH-loss mitochondria in both iMEFs (Fig. 3B and Supplemental Fig. S5B-C) and imCCs (Fig. 3B, especially bottom panel) [75]. We combined this study with independent assessment of three-dimensional mitochondrial volume density using MitoTracker Green staining. This dye binds mitochondria independent of membrane potential (Supplemental Fig. S6A-B). The results are shown in Fig. 3C. These results suggest that SDH-loss cells suffer an overall reduction in cellular mitochondrial volume despite the striking bloating of remaining mitochondria (Fig. 3A).

Our three-dimensional microscopic analysis suggested that *Sdhb*$^{-/-}$ imCCs display a ~ 3-fold volume increase, consistent with the cell diameter differences reported above (Supplemental Fig. S6C-E). Nuclear volume was also increased (Supplemental Fig. S6D). To investigate a potential link between increased nuclear volume and chromosome count [76] we used FISH to determine the number of chromosomes in the four study cell lines, noting that deviation from normal chromosomal count commonly accompanies spontaneous immortalization [77]. Indeed, our results demonstrate striking and heterogeneous polyploidy in both control lines, further increased upon SDH loss (Fig. 3D-E). *Sdhb*$^{-/-}$ imCCs and *Sdhc*$^{-/-}$ iMEFs carry ~ 2.5-fold and ~ 1.8-fold more chromosomes than the expected normal diploid mouse complement of 40 chromosomes, respectively. Initial inspection suggests an increase in chromosome fragments carrying centromeres (Fig. 3E). As previously noted by flow cytometry (Fig. 1E), the total mass of nuclear DNA substantially increased in SDH-loss cells.

Differential metabolic fitness of SDH-loss imCCs vs. iMEFs in normoxia and hypoxia

Loss of SDH function is predicted to disrupt the TCA cycle and reduce the flow of electrons through the mitochondrial electron transport chain, decreasing oxidative phosphorylation. As a result, SDH-loss cells are predicted to demonstrate decreased oxygen consumption and increased reliance on glycolysis [78, 79]. We employed sensitive Seahorse extracellular flux analysis to characterize metabolic phenotypes of control and SDH-loss imCCs and iMEFs in room air (20% oxygen) and more physiologically relevant conditions (5% oxygen).

In 20% O_2, basal oxygen consumption rate (OCR) measurements revealed that while both *Sdhb*$^{-/-}$ imCCs and *Sdhc*$^{-/-}$ iMEFs demonstrated lower resting levels of mitochondrial respiration than their control lines, *Sdhb*$^{-/-}$ imCCs consistently showed higher residual oxidative metabolism than *Sdhc*$^{-/-}$ iMEFs (Fig. 4A). This suggests a distinctive chromaffin cell-specific adaptation to SDH loss, as previously suggested for these cells [29]. This result is also consistent with the absence of lactate accumulation in *Sdhb*$^{-/-}$ imCCs noted above (Fig. 2A). Thus, while both *Sdhb*$^{-/-}$ imCCs and *Sdhc*$^{-/-}$ iMEFs show deficits in oxidative metabolism, the effect is more severe for SDH-loss iMEFs. Interestingly, residual non-mitochondrial oxygen utilization (signal at ~ 70 min in Fig. 4A, B) appears lower for both SDH-loss cell lines than their control counterparts. A plausible explanation for this interesting observation is that dioxygenase intoxication by accumulated succinate in SDH-loss cells blocks non-mitochondrial oxygen utilization by this large family of enzymes [80].

Seahorse studies of oxygen utilization were repeated under physiologically relevant conditions (5% oxygen). Strikingly, basal oxygen utilization by *Sdhb*$^{-/-}$ imCCs under hypoxia became essentially indistinguishable from that of WT *Sdhb*$^{+/+}$ imCCs (Fig. 4B). This indicates much higher basal oxidative fitness for SDH-loss imCCs than SDH-loss iMEFs under physiological oxygen concentratitons. This result again points to the possibility that the chromaffin cell context tolerates SDH loss better than the fibroblast context, supporting the observed tissue specificity of SDH-loss PPGL. Both SDH-loss cell lines are deficient with respect to maximum oxidative capacity following uncoupling with FCCP, suggesting a limited ability to respond to high energy demand (Fig. 4B).

As noted, the previous study of these SDH-loss imCCs by Kľučková et al. [29] attributed residual oxidative capacity of SDH-loss imCC to residual function of mitochondrial Complex I in the absence of SDH (Complex II). To directly test this hypothesis in our systems, we employed Seahorse instrumentation with a modified protocol in permeabilized cells enabling the supply of complex-specific substrates and inhibitors, including rotenone as a specific complex I inhibitor, followed by succinate as a complex II substrate, and concluding with Antimycin A as inhibitor of the entire electron transport chain [29, 55, 81]. This experiment (Fig. 4C-E) was performed in 20% O_2. Importantly, our data show that SDH-loss imCCs, but not SDH-loss iMEFs, substantially preserve Complex I activity and corresponding oxygen utilization, even in the complete absence of complex II activity (Fig. 4C-E). This is a remarkable confirmatory observation given the obviously compromised mitochondrial morphology in SDH-loss imCCs (Fig. 3A).

Strikingly different transcriptomic responses of imCCs and iMEFs to SDH loss

We compared RNA expression in our four cell lines of interest. The cellular response to SDH loss is anticipated to involve activation of cell type-specific signaling

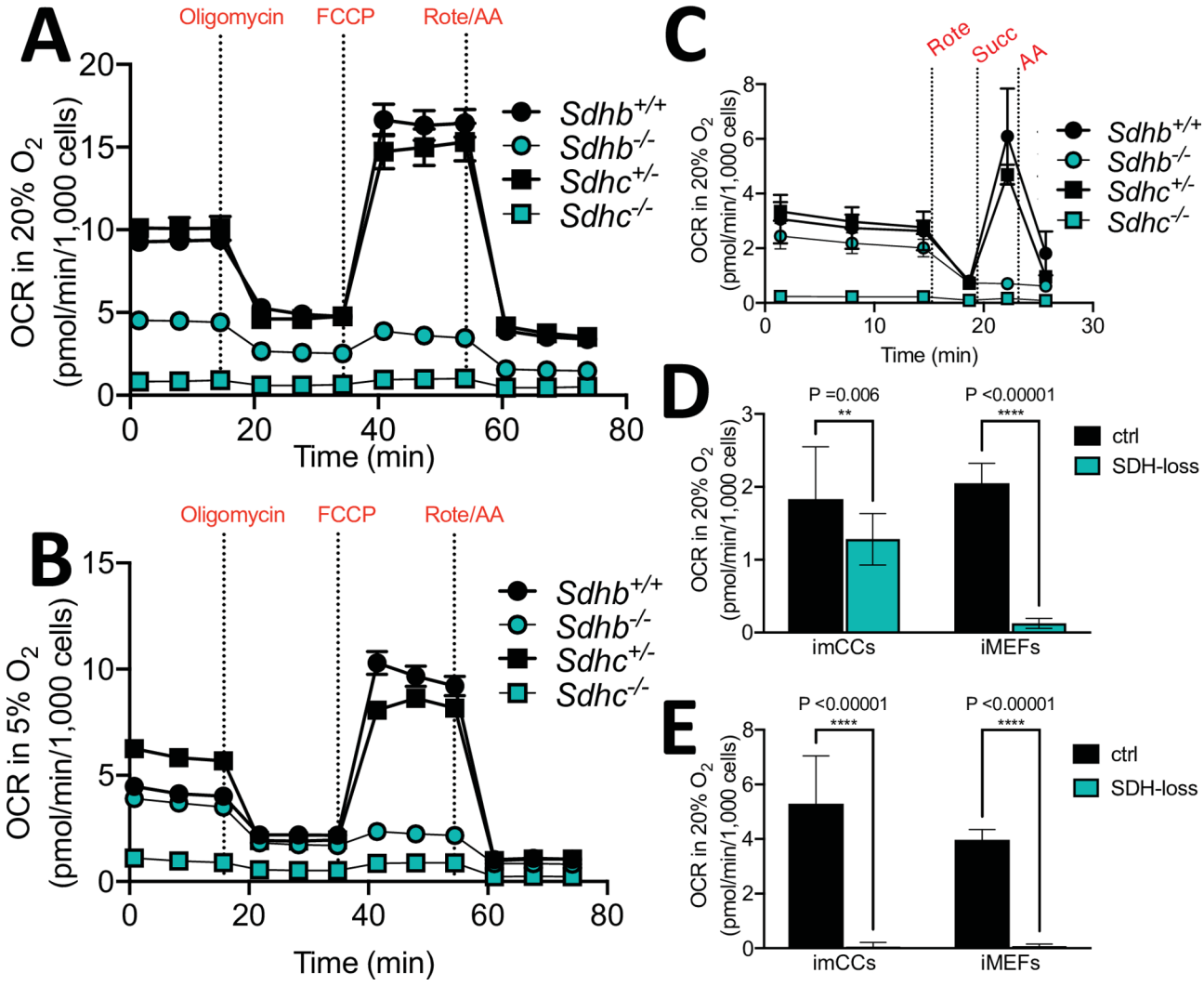

Fig. 4 imCCs, *but not iMEFs maintain substantial metabolic fitness following loss of SDH.* (**A-B**) Seahorse mitochondrial stress test profiles for the indicated cell lines in 20% O_2 (**A**) or 5% O_2 (**B**). Rote/AA: rotenone and antimycin A. (**C**) Complex-specific Seahorse-based assay utilizing Complex I, II and III inhibitors or substrates to assess activities of Complexes I and II in the indicated cell lines. (**D-E**) Bar graphs representing data for Complex I (**D**) or Complex II (**E**) activity from panel C. Seahorse tests were performed in replicates of three ($n = 3$), error bars represent mean ± SEM. *P*-values are calculated using student's t-test and the degree of significance is indicated with number of asterisks

pathways related to stress and metabolic adaptation [82, 83]. Transcriptomic analyses of the four cell lines of interest are shown in Fig. 5 and Supplemental Fig. S8. The volcano plots in Fig. 5AB confirm dramatically altered transcriptomes upon SDH loss, as expected. Interestingly, with the exception of the targeted *Sdhx* genes themselves, SDH knockout did not alter transcription of the other *Sdhx* subunit genes (Fig. 5AB), suggesting that there is not transcriptional feedback regulation from Complex II status to *Sdhx* gene expression. We sought to compare the transcriptional responses of imCCs and iMEFs to SDH loss. These responses were strikingly uncorrelated (Fig. 5C). This result contrasts with the correlation between transcript changes upon SDH loss within a single cell type (for example, imCCs, Fig. 5D). This is an important result, underlining the cell type-specific transcriptional response to SDH loss. The result is further emphasized when a pathway analysis was undertaken to understand altered gene expression in the two cell lines (Supplemental Fig. S8). After accounting for cell type differences in the gene expression, differential gene expression analyses in imCCs and iMEFs detected 679 genes that were overexpressed and showed the same directionality across $Sdhb^{-/-}$ and $Sdhc^{-/-}$ cells and 249 genes that were underexpressed (Supplemental Fig. S9A-D). Quite remarkably, very few upregulated or downregulated pathways are shared in the responses of the two cell types to SDH loss. This suggests a surprising lack of commonality in the response of adrenal-derived cells vs. fibroblasts to SDH loss. This result raises the possibility

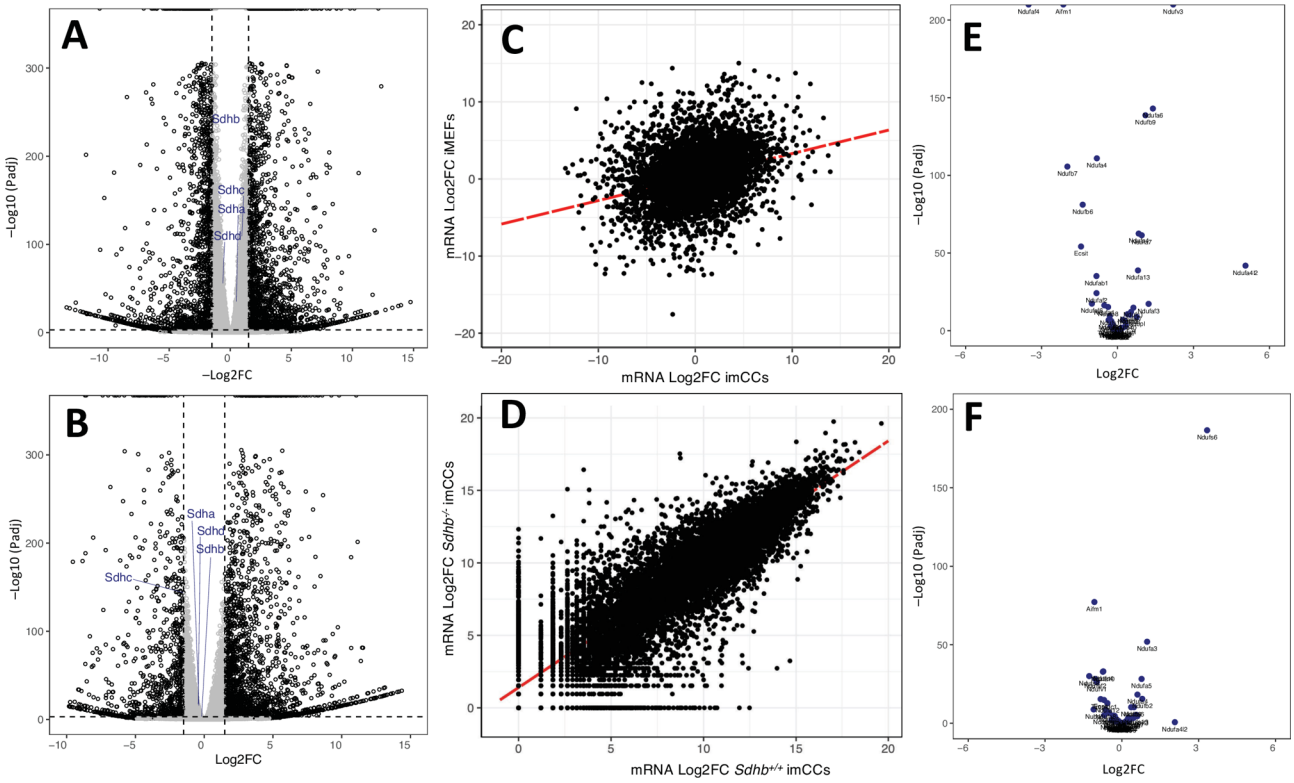

Fig. 5 Distinct transcriptomic changes upon SDH loss in imCCs (**A**) or iMEFs (**B**). Data are displayed as volcano plots where genes shown in back are differentially expressed [*p*-value < 0.05, Log_2(FC) > 1.5]. (**C**) Scatter plot showing relatively poor correlation between Log_2(FC) values for RNA transcripts changed upon SDH loss in imCCs (x-axis) and iMEFs (y-axis). (**D**) For comparison, relatively strong correlation is observed for expressed transcripts between WT imCCs (x-axis) and SDH-loss imCCs (y-axis). E and F. Volcano plots show differential expression of RNAs encoding components of Complex I upon SDH loss in imCCs (**E**) or in iMEFs (**F**). Labelled genes are differentially expressed [*p*-value < 0.05, Log_2(FC) > 1.5]

that adrenal-derived cells are unique in their resilience to SDH loss.

Of particular interest in this regard is the apparent preserved level of oxidative phosphorylation in SDH-loss imCCs. Based on the results presented above, we attribute this at least in part to preserved Complex I activity. We examined the expression of Complex I subunits in response to SDH loss in the two cell types. The results are shown in Fig. 5E, F. It is notable that ~10 Complex I subunits are overexpressed by 2-fold or more upon SDH loss in imCCs, while that number is only ~3 for SDH-loss imCCs. It is likely that one or more of these differentially expressed Complex I subunits may account for sustained Complex I activity in the absence of Complex II in imCCs.

Discussion

Individuals heterozygous for defective variants affecting SDH subunits are at risk for stochastic loss of heterozygosity in susceptible neuroendocrine cells. This triggers development of PPGLs, neuroendocrine tumors that form specifically in the paraganglia, including adrenal chromaffin cells, and extra-adrenal paraganglia found in the carotid bodies and in scattered clusters of the head and neck, abdomen, pelvis, and thorax [63, 84, 85]. The present work continues to examine why SDH loss is tumorigenic, and why tumorigenesis is limited to very specific cell types.

Our study compares characteristics of control and SDH-loss cells derived from mouse adrenal medulla or mouse embryonic fibroblasts. Our comparison is based on cell lines available to the field, and we note that the comparison is imperfect because imCCs suffer SDHB loss while iMEFs suffer SDHC loss. Thus, not only is the cell type different, but the particular SDH subunit insult is different. SDHA carries the active site for succinate oxidation to fumarate, generating $FADH_2$ within the TCA cycle. SDHB contains three iron-sulfur clusters responsible for passing electrons from $FADH_2$ and routing them to membrane-soluble ubiquinone forming ubiquinol among the membrane anchoring SDHC and SDHD subunits [85]. Because all SDH subunits are required for complex stability and for proper function within the TCA cycle and as complex II of mitochondrial electron transport chain [63, 82, 83], we consider that SDHB loss and SDHC loss will have equivalent enzymatic effects. However, this assumption can be challenged. Stochastic somatic LOH results in loss of SDH tumor suppressor

function in vulnerable cells of heterozygous individuals [66, 85–87]. While the enzymatic results of SDHB and SDHC loss should theoretically be identical (total loss of SDH function), subtle differences in residual SDH subunit inventory and activity could contribute to other differences between SDHB-loss imCCs and SDHC-loss iMEFs. For example, it remains a mysterious feature of SDH-deficient PPGL that SDHB loss appears more clinically penetrant than SDHC loss [65, 88]. Possible mechanisms continue to be pursued [88–90]. Our goal here has been to explore mechanisms contributing to cell type-specific vulnerability to tumorigenesis after SDH loss.

Pathology in cellular energy machinery is reasonably expected to affect vital processes such as cell division, mobility, adhesion, cytoskeletal rearrangement, post-translational protein modifications, epigenetic control and metabolite composition lose homeostasis [91–93]. Our present results suggest that common responses to SDH loss shared between imCCs and iMEFs include increased cell size and slowed proliferation with cell cycle alterations (Fig. 1A-E). Both cell types also accumulate succinate to a striking degree (Fig. 2B-C), confirming that (i) SDH function is compromised and (ii) that SDHB and SDHC are equally important for SDH enzyme activity. Intriguingly, SDH-loss iMEFs showed relatively normal levels of TCA metabolites isocitrate, 2-hydroxyglutarate and glutamate, but uniquely accumulated lactate. These results suggest a shift towards glycolysis in *Sdhc*$^{-/-}$ iMEFs. We note that our ECAR measurements were not sufficiently sensitive to detect this effect (Supplemental Fig. S7). Additionally, we show that a hallmark of SDHx-loss cells, namely inhibition of dioxygenases such as JMJD demethylases is detectable in SDH-loss cells (Fig. 2D), confirming a canonical response in both cell types. We find that HIF transcription factor subunit responses to SDH loss in these cells are more complex (Fig. 2E).

In agreement with previously observed human tumor pathology, ultrastructure analysis (Fig. 3A) suggests shared aspects of mitochondrial pathology in SDH-loss imCCs and iMEFs, with the former showing more profound mitochondrial defects [94–96]. These results were coupled with abnormal reorganization of actin filaments with actin-enclosed mitochondria (Fig. 3B) [75]. Electron microscopy demonstrates severe alteration in mitochondrial morphology particularly in SDH-loss imCC. The swollen residual mitochondria demlnstrate only traces of cristae [97] (Fig. 3A). Defective mitochondria in SDH-loss imCC often include single electron-dense condensed bodies of unknown origin (Fig. 3A, bottom right). It is tempting to speculate that these deposits may correspond to nucleoid material. Our additional three-dimensional microscopy-based measurements suggest an overall decrease in mitochondrial volume density for SDH-loss cells. Previously published volume measurements with this imCC model reported increased volume per mitochondrion [29]. We suggest, based on their results as well as our own (Fig. 3A, D), that both SDH-loss models suffer an overall loss of mitochondrial count, with remaining mitochondria appearing pathologically swollen (Fig. 3A).

It remains unknown how our observations of profound succinate accumulation relate to previous studies of inflammatory responses [98]. Pro-inflammatory pathways may become upregulated at a critical commitment point involving mitochondria prior to apoptosis. As such, SDH loss presumably inhibits various normal roles of mitochondria [99]. While pathological mitochondrial morphology is observed in both SDH-loss imCCs and SDH-loss iMEFs, SDH-loss imCC appear more strongly affected (Fig. 3A).

Importantly, our findings confirm that *Sdhb*$^{-/-}$ imCCs maintain a higher basal OCR than *Sdhc*$^{-/-}$ iMEFs, in room air. This is consistent with the previous hypothesis [29] that chromaffin cells maintain residual mitochondrial Complex I in the absence of SDH (Complex II), whereas fibroblasts such as SDH-loss iMEFs do not [29]. Using a complex-specific Seahorse analysis, we directly confirm this residual Complex I activity in SDHB-loss imCCs (Fig. 4C-D). This is paradoxical because it suggests greater residual Complex I activity in the context of mitochondria that have more demonstrably severe pathology (SDH-loss imCCs) than in cells with less profoundly deranged mitochondria (SDH-loss iMEFs) (Fig. 3A).

The observation that *Sdhb*$^{-/-}$ imCCs appear more metabolically fit than *Sdhc*$^{-/-}$ iMEFs is consistent with the hypothesis that it is this residual metabolic fitness that makes chromaffin cells uniquely susceptible to PPGL tumorigenesis because of their ability to better proliferate after SDH loss. This possibility is particularly striking in light of our findings under physiologically-relevant 5% O_2 conditions where *Sdhb*$^{-/-}$ imCCs appeared as metabolically competent as WT imCCs prior to the addition of FCCP uncoupling agent (Fig. 4B). *These findings suggest a higher and physiologically-relevant adaptability of imCCs to SDH loss relative to Sdhc*$^{-/-}$*iMEFs.*

Finally, the results of our RNA sequencing studies clearly demonstrate that transcriptional responses to SDH loss are cell type-specific, revealing strikingly different patterns between the two tested cases (Fig. 5). Though some common themes can be detected, the overall picture is one of idiosyncratic responses to SDH loss in each cell type. This result suggests the crucial importance of cell context in determining whether loss of the TCA cycle is tumorigenic.

Abbreviations

ECAR	Extracellular acidification rate
FCCP	Carbonyl cyanide 4-(trifluoromethoxy)phenylhydrazone
FISH	Fluorescent in situ hybridization

imCCs	Immortalized mouse chromaffin cells
iMEFs	Immortalized mouse embryonic fibroblasts
LOH	Loss of heterozygosity
MEFs	Mouse embryonic fibroblasts
mPMS	1-methoxy-5-methylphenazinium methyl sulfate
NBT	Nitro blue tetrazolium
NBT_{dfz}	Nitro blue tetrazolium diformazan
OCR	Oxygen consumption rate
PPGL	Pheochromocytoma and paraganglioma
SDH	Succinate dehydrogenase
TCA	Tricarboxylic acid

Supplementary Information

The online version contains supplementary material available at https://doi.org/10.1186/s40170-024-00369-9.

Supplementary Material 1

Acknowledgements
The authors acknowledge the technical assistance of the staff of the Mayo Clinic Metabolomics Core Facility, Mayo Clinic Division of Laboratory Genetics and Genomics Laboratory, as well as the Mayo Clinic Microscopy and Cell Analysis Core for experimental and technical support. Members of the Maher laboratory are acknowledged. The Mayo Clinic Cytogenetics Core, including Patricia T. Greipp, Carolyn Brandt, Troy Gliem, and Ryan Knudson are thanked for their technical assistance with karyotyping analysis. We thank Drs. Taro Hitosugi and Scott Kaufmann for generously sharing reagents and equipment. Some figures were created using BioRender.com.

Author contributions
FJAK, LJM, GS, and CF designed the experiments; FJAK, SMB, BAW, YZ, and SXZ performed the experiments; FJAK, SXZ, YZ, SMB, and CMdeAC analyzed data; FJAK and LJM wrote the manuscript; JF provided research materials and editing.

Funding
This work was supported by generous funding from the Paradifference Foundation, NIH grant R21CA266999 (LJM), the Mayo Clinic Graduate School of Biomedical Sciences (FJAK, BAW, SXZ), and NIH institutional training grant T32 GM145408 (SXZ). C. Folmes and Y. Zhu are funded by NIH grant HL121079, the Anne Dash Weinman Fund in Cardiovascular Disease Research Honoring Steven J. Lester, M.D., the Nasser Al-Rashid Fund for Research in Cardiovascular Diseases, and the Roubos Family Fund in Research. S. Mahadev-Bhat and G. Sieck are supported by NIH grant R01-HL157984 (National Heart, Lung, and Blood Institute). Data produced in the Mayo Clinic Cytogenetics Core Laboratory is supported, in part, by the Mayo Clinic Comprehensive Cancer Center Grant, funded by the NCI grant P30CA15083.

Data availability
RNA sequencing data have been deposited in the Gene Expression Omnibus (GEO) database as GSE263778.

Declarations

Competing interests
The authors declare no competing interests.

Data deposition
RNA sequencing data have been deposited in the Gene Expression Omnibus (GEO) database as GSE263778.

Author details
[1]Mayo Clinic Graduate School of Biomedical Sciences, Mayo Clinic College of Medicine and Science, Rochester, MN, USA
[2]Department of Biochemistry and Molecular Biology, Mayo Clinic College of Medicine and Science, 200 First St. SW, Rochester, MN 55905, USA
[3]Department of Physiology and Biomedical Engineering, Mayo Clinic, Rochester, MN, USA
[4]Department of Biochemistry and Molecular Biology, Mayo Clinic, Scottsdale, AZ, USA
[5]Department of Molecular Pharmacology and Experimental Therapeutics, Mayo Clinic, Rochester, MN, USA
[6]Medical Scientist Training Program, Mayo Clinic Alix School of Medicine, Mayo Clinic, Rochester, MN, USA
[7]Inserm, Centre de recherche des Cordeliers, Université Paris-Cité, Sorbonne Université, Equipe Labellisée Ligue contre le Cancer, Paris 75006, France

Received: 18 June 2024 / Accepted: 18 December 2024
Published online: 23 December 2024

References

1. Huang S, Millar AH. Succinate dehydrogenase: the complex roles of a simple enzyme. Curr Opin Plant Biol. 2013;16(3):344–9.
2. Rutter J, Winge DR, Schiffman JD. Succinate dehydrogenase - assembly, regulation and role in human disease. Mitochondrion. 2010;10(4):393–401.
3. Sharma P, Maklashina E, Cecchini G, Iverson TM. The roles of SDHAF2 and dicarboxylate in covalent flavinylation of SDHA, the human complex II flavoprotein. Proc Natl Acad Sci U S A. 2020;117(38):23548–56.
4. Bezawork-Geleta A, Dong L, Rohlena J, Neuzil J. The Assembly factor SDHAF2 is dispensable for Flavination of the Catalytic Subunit of mitochondrial complex II in breast Cancer cells. J Biol Chem. 2016;291(41):21414–20.
5. Rasheed M, Tarjan G. Succinate dehydrogenase complex: an updated review. Arch Pathol Lab Med. 2018;142(12):1564–70.
6. Frazier AE, Thorburn DR, Compton AG. Mitochondrial energy generation disorders: genes, mechanisms, and clues to pathology. J Biol Chem. 2019;294(14):5386–95.
7. Evenepoel L, Papathomas TG, Krol N, Korpershoek E, de Krijger RR, Persue A, Dinjens W. Toward an improved definition of the genetic and tumor spectrum associated with SDH germ-line mutations. Genet Med. 2015;8:610–20.
8. Goncalves J, Moog S, Morin A, Gentric G, Muller S, Morrell AP, Kluckova K, Stewart TJ, Andoniadou CL, Lussey-Lepoutre C, et al. Loss of SDHB promotes Dysregulated Iron Homeostasis, oxidative stress, and sensitivity to Ascorbate. Cancer Res. 2021;81(13):3480–94.
9. Rustin P, Munnich A, Rotig A. Succinate dehydrogenase and human diseases: new insights into a well-known enzyme. Eur J Hum Genet. 2002;10(5):289–91.
10. McEvoy CR, Koe L, Choong DY, Leong HS, Xu H, Karikios D, Plew JD, Prall OW, Fellowes AP, Fox SB. SDH-deficient renal cell carcinoma associated with biallelic mutation in succinate dehydrogenase A: comprehensive genetic profiling and its relation to therapy response. NPJ Precis Oncol. 2018;2:9.
11. Aghamir SMK, Heshmat R, Ebrahimi M, Ketabchi SE, Parichehreh Dizaji S, Khatami F. The impact of Succinate dehydrogenase gene (SDH) mutations in renal cell carcinoma (RCC): a systematic review. Onco Targets Ther. 2019;12:7929–40.
12. Hart ML, Quon E, Vigil ABG, Engstrom IA, Newsom OJ, Davidsen K, Hoellerbauer P, Carlisle SM, Sullivan LB. Mitochondrial redox adaptations enable alternative aspartate synthesis in SDH-deficient cells. Elife 2023, 12.
13. Bardella C, Pollard PJ, Tomlinson I. SDH mutations in cancer. Biochim Biophys Acta. 2011;1807(11):1432–43.
14. She Y, Mao A, Li F, Wei X. P5CR1 protein expression and the effect of gene-silencing on lung adenocarcinoma. PeerJ. 2019;7:e6934.
15. Eijkelenkamp K, Osinga TE, Links TP, van der Horst-Schrivers ANA. Clinical implications of the oncometabolite succinate in SDHx-mutation carriers. Clin Genet. 2020;97(1):39–53.
16. Moreno C, Santos RM, Burns R, Zhang WC. Succinate dehydrogenase and ribonucleic acid networks in Cancer and Other diseases. Cancers (Basel) 2020, 12(11).
17. Fan F, Sam R, Ryan E, Alvarado K, Villa-Cuesta E. Rapamycin as a potential treatment for succinate dehydrogenase deficiency. Heliyon. 2019;5(2):e01217.
18. Casas-Benito A, Martinez-Herrero S, Martinez A. Succinate-Directed approaches for Warburg Effect-Targeted Cancer Management, an alternative to current treatments? Cancers (Basel) 2023, 15(10).
19. Selak MA, Armour SM, MacKenzie ED, Boulahbel H, Watson DG, Mansfield KD, Pan Y, Simon MC, Thompson CB, Gottlieb E. Succinate links TCA cycle dysfunction to oncogenesis by inhibiting HIF-alpha prolyl hydroxylase. Cancer Cell. 2005;7(1):77–85.
20. Sreedhar A, Wiese EK, Hitosugi T. Enzymatic and metabolic regulation of lysine succinylation. Genes Dis. 2020;7(2):166–71.

21. Kubatzky KF, Gao Y, Yu D. Post-translational modulation of cell signalling through protein succinylation. Explor Target Antitumor Ther. 2023;4(6):1260–85.
22. Pacak K, Taieb D. Pheochromocytoma (PHEO) and Paraganglioma (PGL). Cancers (Basel) 2019, 11(9).
23. Kastriti ME, Kameneva P, Kamenev D, Dyachuk V, Furlan A, Hampl M, Memic F, Marklund U, Lallemend F, Hadjab S, et al. Schwann Cell Precursors Generate the Majority of Chromaffin Cells in Zuckerkandl Organ and some sympathetic neurons in Paraganglia. Front Mol Neurosci. 2019;12:6.
24. Taieb D, Kaliski A, Boedeker CC, Martucci V, Fojo T, Adler JR Jr., Pacak K. Current approaches and recent developments in the management of head and neck paragangliomas. Endocr Rev. 2014;35(5):795–819.
25. Alrezk R, Suarez A, Tena I, Pacak K. Update of Pheochromocytoma syndromes: Genetics, biochemical evaluation, and imaging. Front Endocrinol (Lausanne). 2018;9:515.
26. Armstrong N, Storey CM, Noll SE, Margulis K, Soe MH, Xu H, Yeh B, Fishbein L, Kebebew E, Howitt BE, et al. SDHB knockout and succinate accumulation are insufficient for tumorigenesis but dual SDHB/NF1 loss yields SDHx-like pheochromocytomas. Cell Rep. 2022;38(9):110453.
27. Her YF, Maher LJ. 3rd: Succinate Dehydrogenase Loss in Familial Paraganglioma: Biochemistry, Genetics, and Epigenetics. *Int J Endocrinol* 2015, 2015:296167.
28. Powers JF, Cochran B, Baleja JD, Sikes HD, Pattison AD, Zhang X, Lomakin I, Shepard-Barry A, Pacak K, Moon SJ, et al. A xenograft and cell line model of SDH-deficient pheochromocytoma derived from Sdhb+/- rats. Endocr Relat Cancer. 2020;27(10):X9–10.
29. Kluckova K, Thakker A, Vettore L, Escribano-Gonzalez C, Hindshaw RL, Tearle JLE, Goncalves J, Kaul B, Lavery GG, Favier J, Tennant DA. Succinate dehydrogenase deficiency in a chromaffin cell model retains metabolic fitness through the maintenance of mitochondrial NADH oxidoreductase function. FASEB J. 2020;34(1):303–15.
30. Letouze E, Martinelli C, Loriot C, Burnichon N, Abermil N, Ottolenghi C, Janin M, Menara M, Nguyen AT, Benit P, et al. SDH mutations establish a hypermethylator phenotype in paraganglioma. Cancer Cell. 2013;23(6):739–52.
31. Kolski-Andreaco A, Cai H, Currle DS, Chandy KG, Chow RH. Mouse adrenal chromaffin cell isolation. J Vis Exp 2007(2):129.
32. Smestad J, Hamidi O, Wang L, Holte MN, Khazal FA, Erber L, Chen Y, Maher LJ. 3rd: characterization and metabolic synthetic lethal testing in a new model of SDH-loss familial pheochromocytoma and paraganglioma. Oncotarget. 2018;9(5):6109–27.
33. Khazal FA, Holte MN, Bolon B, White TA, LeBrasseur N, Iii LJM. A conditional mouse model of complex II deficiency manifesting as Leigh-Like syndrome. FASEB J. 2019;33(12):13189–201.
34. Dutta T, Kudva YC, Persson XM, Schenck LA, Ford GC, Singh RJ, Carter R, Nair KS. Impact of Long-Term Poor and Good Glycemic Control on Metabolomics Alterations in type 1 Diabetic people. J Clin Endocrinol Metab. 2016;101(3):1023–33.
35. Wilkins J, Sakrikar D, Petterson XM, Lanza IR, Trushina E. A comprehensive protocol for multiplatform metabolomics analysis in patient-derived skin fibroblasts. Metabolomics. 2019;15(6):83.
36. Hinton A Jr., Katti P, Christensen TA, Mungai M, Shao J, Zhang L, Trushin S, Alghanem A, Jaspersen A, Geroux RE, et al. A Comprehensive Approach to Sample Preparation for Electron Microscopy and the Assessment of mitochondrial morphology in tissue and cultured cells. Adv Biol (Weinh). 2023;7(10):e2200202.
37. Nolte J, Pette D. Microphotometric determination of enzyme activity in single cells in cryostat section. II. Succinate dehydrogenase, lactate dehydrogenase and triosephosphate dehydrogenase activities in red, intermediate and white fibers of soleus and rectus femoris muscles of rat. J Histochem Cytochem. 1972;20(8):577–82.
38. Sieck GC, Sacks RD, Blanco CE, Edgerton VR. SDH activity and cross-sectional area of muscle fibers in cat diaphragm. J Appl Physiol (1985). 1986;60(4):1284–92.
39. Sieck GC, Sacks RD, Blanco CE. Absence of regional differences in the size and oxidative capacity of diaphragm muscle fibers. J Appl Physiol (1985). 1987;63(3):1076–82.
40. Sieck GC, Lewis MI, Blanco CE. Effects of undernutrition on diaphragm fiber size, SDH activity, and fatigue resistance. J Appl Physiol (1985). 1989;66(5):2196–205.
41. Blanco CE, Sieck GC, Edgerton VR. Quantitative histochemical determination of succinic dehydrogenase activity in skeletal muscle fibres. Histochem J. 1988;20(4):230–43.
42. Enad JG, Fournier M, Sieck GC. Oxidative capacity and capillary density of diaphragm motor units. J Appl Physiol (1985). 1989;67(2):620–7.
43. Sieck GC, Blanco CE. Postnatal changes in the distribution of succinate dehydrogenase activities among diaphragm muscle fibers. Pediatr Res. 1991;29(6):586–93.
44. Sieck GC, Cheung TS, Blanco CE. Diaphragm capillarity and oxidative capacity during postnatal development. J Appl Physiol (1985). 1991;70(1):103–11.
45. Lewis MI, Monn SA, Sieck GC. Effect of corticosteroids on diaphragm fatigue, SDH activity, and muscle fiber size. J Appl Physiol (1985). 1992;72(1):293–301.
46. Johnson BD, Sieck GC. Activation-induced reduction of SDH activity in diaphragm muscle fibers. J Appl Physiol (1985). 1993;75(6):2689–95.
47. Blanco CE, Micevych PE, Zhan WZ, Sieck GC. Succinate dehydrogenase activity of sexually dimorphic muscles of rats. J Appl Physiol (1985). 1995;78(6):2147–52.
48. Proctor DN, Sinning WE, Walro JM, Sieck GC, Lemon PW. Oxidative capacity of human muscle fiber types: effects of age and training status. J Appl Physiol (1985). 1995;78(6):2033–8.
49. Sieck GC, Fournier M, Prakash YS, Blanco CE. Myosin phenotype and SDH enzyme variability among motor unit fibers. J Appl Physiol (1985). 1996;80(6):2179–89.
50. Mahadev Bhat S, Yap JQ, Ramirez-Ramirez OA, Delmotte P, Sieck GC. Cell-based measurement of mitochondrial function in human airway smooth muscle cells. Int J Mol Sci 2023, 24(14).
51. Sieck GC, Zhan WZ, Prakash YS, Daood MJ, Watchko JF. SDH and actomyosin ATPase activities of different fiber types in rat diaphragm muscle. J Appl Physiol (1985). 1995;79(5):1629–39.
52. Fogarty MJ, Marin Mathieu N, Mantilla CB, Sieck GC. Aging reduces succinate dehydrogenase activity in rat type IIx/IIb diaphragm muscle fibers. J Appl Physiol (1985). 2020;128(1):70–7.
53. Brown AD, Fogarty MJ, Davis LA, Dasgupta D, Mantilla CB, Sieck GC. Mitochondrial adaptations to inactivity in diaphragm muscle fibers. J Appl Physiol (1985). 2022;133(1):191–204.
54. Brown AD, Fogarty MJ, Sieck GC. Mitochondrial morphology and function varies across diaphragm muscle fiber types. Respir Physiol Neurobiol. 2022;295:103780.
55. Tsogtbaatar E, Minter-Dykhouse K, Saarinen A, Folmes CDL. Extracellular flux analysis of mitochondrial function in pluripotent stem cells. Methods Mol Biol. 2022;2429:85–102.
56. Dobin A, Davis CA, Schlesinger F, Drenkow J, Zaleski C, Jha S, Batut P, Chaisson M, Gingeras TR. STAR: ultrafast universal RNA-seq aligner. Bioinformatics. 2013;29(1):15–21.
57. Liao Y, Smyth GK, Shi W. featureCounts: an efficient general purpose program for assigning sequence reads to genomic features. Bioinformatics. 2014;30(7):923–30.
58. Love MI, Huber W, Anders S. Moderated estimation of Fold change and dispersion for RNA-seq data with DESeq2. Genome Biol. 2014;15(12):550.
59. Gu Z, Eils R, Schlesner M. Complex heatmaps reveal patterns and correlations in multidimensional genomic data. Bioinformatics. 2016;32(18):2847–9.
60. Lussey-Lepoutre C, Hollinshead KE, Ludwig C, Menara M, Morin A, Castro-Vega LJ, Parker SJ, Janin M, Martinelli C, Ottolenghi C, et al. Loss of succinate dehydrogenase activity results in dependency on pyruvate carboxylation for cellular anabolism. Nat Commun. 2015;6:8784.
61. Kuo CC, Wu JY, Wu KK. Cancer-derived extracellular succinate: a driver of cancer metastasis. J Biomed Sci. 2022;29(1):93.
62. Atallah R, Olschewski A, Heinemann A. Succinate at the Crossroad of Metabolism and Angiogenesis: Roles of SDH, HIF1alpha and SUCNR1. *Biomedicines* 2022, 10(12).
63. Gill AJ. Succinate dehydrogenase (SDH)-deficient neoplasia. Histopathology. 2018;72(1):106–16.
64. Van Vranken JG, Na U, Winge DR, Rutter J. Protein-mediated assembly of succinate dehydrogenase and its cofactors. Crit Rev Biochem Mol Biol. 2015;50(2):168–80.
65. Moog S, Lussey-Lepoutre C, Favier J. Epigenetic and metabolic reprogramming of SDH-deficient paragangliomas. Endocr Relat Cancer. 2020;27(12):R451–63.
66. Bandara AB, Drake JC, Brown DA. Complex II subunit SDHD is critical for cell growth and metabolism, which can be partially restored with a synthetic ubiquinone analog. BMC Mol Cell Biol. 2021;22(1):35.
67. Murad H, Hawat M, Ekhtiar A, AlJapawe A, Abbas A, Darwish H, Sbenati O, Ghannam A. Induction of G1-phase cell cycle arrest and apoptosis pathway in MDA-MB-231 human breast cancer cells by sulfated polysaccharide extracted from Laurencia papillosa. Cancer Cell Int. 2016;16:39.

68. Pan Z, Luo Y, Xia Y, Zhang X, Qin Y, Liu W, Li M, Liu X, Zheng Q, Li D. Cinobufagin induces cell cycle arrest at the S phase and promotes apoptosis in nasopharyngeal carcinoma cells. Biomed Pharmacother. 2020;122:109763.
69. Matlac DM, Hadrava Vanova K, Bechmann N, Richter S, Folberth J, Ghayee HK, Ge GB, Abunimer L, Wesley R, Aherrahrou R, et al. Succinate mediates tumorigenic effects via Succinate Receptor 1: potential for new targeted treatment strategies in Succinate Dehydrogenase Deficient Paragangliomas. Front Endocrinol (Lausanne). 2021;12:589451.
70. Rogatzki MJ, Ferguson BS, Goodwin ML, Gladden LB. Lactate is always the end product of glycolysis. Front Neurosci. 2015;9:22.
71. Losman JA, Koivunen P, Kaelin WG Jr. 2-Oxoglutarate-dependent dioxygenases in cancer. Nat Rev Cancer. 2020;20(12):710–26.
72. Her YF, Nelson-Holte M, Maher LJ 3. Oxygen concentration controls epigenetic effects in models of familial paraganglioma. PLoS ONE. 2015;10(5):e0127471.
73. Chang YL, Hsieh MH, Chang WW, Wang HY, Lin MC, Wang CP, Lou PJ, Teng SC. Instability of succinate dehydrogenase in SDHD polymorphism connects reactive oxygen species production to nuclear and mitochondrial genomic mutations in yeast. Antioxid Redox Signal. 2015;22(7):587–602.
74. D'Antongiovanni V, Martinelli S, Richter S, Canu L, Guasti D, Mello T, Romagnoli P, Pacak K, Eisenhofer G, Mannelli M, Rapizzi E. The microenvironment induces collective migration in SDHB-silenced mouse pheochromocytoma spheroids. Endocr Relat Cancer. 2017;24(10):555–64.
75. Hunt M, Torres M, Bachar-Wikstrom E, Wikstrom JD. Multifaceted roles of mitochondria in wound healing and chronic wound pathogenesis. Front Cell Dev Biol. 2023;11:1252318.
76. Prisant N, Escalier D, Soufir JC, Morillon M, Schoevaert D, Misrahi M, Tachdjian G. Ultrastructural nuclear defects and increased chromosome aneuploidies in spermatozoa with elongated heads. Hum Reprod. 2007;22(4):1052–9.
77. Williams BR, Prabhu VR, Hunter KE, Glazier CM, Whittaker CA, Housman DE, Amon A. Aneuploidy affects proliferation and spontaneous immortalization in mammalian cells. Science. 2008;322(5902):703–9.
78. Tabebi M, Kumar Dutta R, Skoglund C, Soderkvist P, Gimm O. Loss of SDHB induces a metabolic switch in the hPheo1 cell line toward enhanced OXPHOS. Int J Mol Sci 2022, 23(1).
79. Ricci L, Stanley FU, Eberhart T, Mainini F, Sumpton D, Cardaci S. Pyruvate transamination and NAD biosynthesis enable proliferation of succinate dehydrogenase-deficient cells by supporting aerobic glycolysis. Cell Death Dis. 2023;14(7):403.
80. Zhang Y, Zhang M, Zhu W, Yu J, Wang Q, Zhang J, Cui Y, Pan X, Gao X, Sun H. Succinate accumulation induces mitochondrial reactive oxygen species generation and promotes status epilepticus in the kainic acid rat model. Redox Biol. 2020;28:101365.
81. Ma X, Jin M, Cai Y, Xia H, Long K, Liu J, Yu Q, Yuan J. Mitochondrial electron transport chain complex III is required for antimycin A to inhibit autophagy. Chem Biol. 2011;18(11):1474–81.
82. Indio V, Schipani A, Nannini M, Urbini M, Rizzo A, De Leo A, Altimari A, Di Scioscio V, Messelodi D, Tarantino G et al. Gene expression Landscape of SDH-Deficient gastrointestinal stromal tumors. J Clin Med 2021, 10(5).
83. You M, Xie Z, Zhang N, Zhang Y, Xiao D, Liu S, Zhuang W, Li L, Tao Y. Signaling pathways in cancer metabolism: mechanisms and therapeutic targets. Signal Transduct Target Ther. 2023;8(1):196.
84. Suzuki D, Meguro S, Watanabe Y, Kawai T, Kyokane T, Aoshima Y, Enomoto Y, Kawasaki H, Yagi H, Kosugi I, et al. Incidentally discovered mesenteric paraganglia as large as a lymph node in the sigmoid mesocolon, a possible origin of mesenteric paraganglioma. Pathol Int. 2020;70(7):476–8.
85. Oudijk L, Gaal J, de Krijger RR. The role of immunohistochemistry and molecular analysis of Succinate dehydrogenase in the diagnosis of endocrine and non-endocrine tumors and related syndromes. Endocr Pathol. 2019;30(1):64–73.
86. Renkema GH, Wortmann SB, Smeets RJ, Venselaar H, Antoine M, Visser G, Ben-Omran T, van den Heuvel LP, Timmers HJ, Smeitink JA, Rodenburg RJ. SDHA mutations causing a multisystem mitochondrial disease: novel mutations and genetic overlap with hereditary tumors. Eur J Hum Genet. 2015;23(2):202–9.
87. Cao K, Xu J, Cao W, Wang X, Lv W, Zeng M, Zou X, Liu J, Feng Z. Assembly of mitochondrial succinate dehydrogenase in human health and disease. Free Radic Biol Med. 2023;207:247–59.
88. Bezawork-Geleta A, Wen H, Dong L, Yan B, Vider J, Boukalova S, Krobova L, Vanova K, Zobalova R, Sobol M, et al. Alternative assembly of respiratory complex II connects energy stress to metabolic checkpoints. Nat Commun. 2018;9(1):2221.
89. Bayley JP, Devilee P. Hypothesis: why different types of SDH Gene variants cause divergent tumor phenotypes. Genes (Basel) 2022, 13(6).
90. Gruber LM, Hart SN, Maher Iii LJ. Succinate dehydrogenase variants in paraganglioma: why are b subunit variants 'bad'? Endocr Oncol. 2023;3(1):e220093.
91. Flood D, Lee ES, Taylor CT. Intracellular energy production and distribution in hypoxia. J Biol Chem. 2023;299(9):105103.
92. Neves JB, Roberts K, Nguyen JS, El Sheikh S, Tran-Dang MA, Horsfield C, Mumtaz F, Campbell P, Stauss H, Tran MGB, Mitchell T. Defining the origin, evolution, and immune composition of SDH-deficient renal cell carcinoma. iScience. 2022;25(11):105389.
93. Cornejo KM, Lu M, Yang P, Wu S, Cai C, Zhong WD, Olumi A, Young RH, Wu CL. Succinate dehydrogenase B: a new prognostic biomarker in clear cell renal cell carcinoma. Hum Pathol. 2015;46(6):820–6.
94. Douwes Dekker PB, Hogendoorn PC, Kuipers-Dijkshoorn N, Prins FA, van Duinen SG, Taschner PE, van der Mey AG, Cornelisse CJ. SDHD mutations in head and neck paragangliomas result in destabilization of complex II in the mitochondrial respiratory chain with loss of enzymatic activity and abnormal mitochondrial morphology. J Pathol. 2003;201(3):480–6.
95. Housley SL, Lindsay RS, Young B, McConachie M, Mechan D, Baty D, Christie L, Rahilly M, Qureshi K, Fleming S. Renal carcinoma with giant mitochondria associated with germ-line mutation and somatic loss of the succinate dehydrogenase B gene. Histopathology. 2010;56(3):405–8.
96. Ishii T, Yasuda K, Akatsuka A, Hino O, Hartman PS, Ishii N. A mutation in the SDHC gene of complex II increases oxidative stress, resulting in apoptosis and tumorigenesis. Cancer Res. 2005;65(1):203–9.
97. Jezek P, Jaburek M, Holendova B, Engstova H, Dlaskova A. Mitochondrial cristae morphology reflecting metabolism, superoxide formation, Redox Homeostasis, and Pathology. Antioxid Redox Signal. 2023;39(10–12):635–83.
98. Zhang W, Lang R. Succinate metabolism: a promising therapeutic target for inflammation, ischemia/reperfusion injury and cancer. Front Cell Dev Biol. 2023;11:1266973.
99. Vringer E, Tait SWG. Mitochondria and cell death-associated inflammation. Cell Death Differ. 2023;30(2):304–12.

Publisher's note